

# Chapter 6

## Spectroscopy of Small and Large Biomolecular Ions in Helium-Nanodroplets



**Eike Mucha, Daniel Thomas, Maike Lettow, Gerard Meijer, Kevin Pagel, and Gert von Helden**

**Abstract** A vast number of experiments have now shown that helium nanodroplets are an exemplary cryogenic matrix for spectroscopic investigations. The experimental techniques are well established and involve in most cases the pickup of evaporated neutral species by helium droplets. These techniques have been extended within our research group to enable nanodroplet pickup of anions or cations stored in an ion trap. By using electrospray ionization (ESI) in combination with modern mass spectrometric methods to supply ions to the trap, an immense variety of mass-to-charge selected species can be doped into the droplets and spectroscopically investigated. We have combined this droplet doping methodology with IR action spectroscopy to investigate anions and cations ranging in size from a few atoms to proteins that consist of thousands of atoms. Herein, we show examples of small complexes of fluoride anions ( $F^-$ ) with  $CO_2$  and  $H_2O$  and carbohydrate molecules. In the case of the small complexes, novel compounds could be identified, and quantum chemistry can in some instances quantitatively explain the results. For biologically relevant complex carbohydrate molecules, the IR spectra are highly diagnostic and allow the differentiation of species that would be difficult or impossible to identify by more conventional methods.

---

E. Mucha · D. Thomas · M. Lettow · G. Meijer · K. Pagel · G. von Helden (✉)  
Fritz-Haber-Institut der Max-Planck-Gesellschaft, Faradayweg 4-6, 14105 Berlin, Germany  
e-mail: [helden@fhi-berlin.mpg.de](mailto:helden@fhi-berlin.mpg.de)

D. Thomas  
Department of Chemistry, University of Rhode Island, Kingston, RI 02881, USA

K. Pagel  
Institut für Chemie und Biochemie, Freie Universität Berlin, Arnimallee 22, 14195 Berlin, Germany

## 6.1 Introduction

Experimental probes based on light-matter interactions have proven to be among the most effective means to elucidate molecular structure and dynamics. In early experiments, continuous-wave light sources were used to acquire information on the energy levels and structures of molecules in stationary states. Although knowing the equilibrium structures of molecules is crucial, many important processes such as excited state decay or chemical reactions involve electronic and nuclear dynamics as well as energy flow between various degrees of freedom. To investigate such processes, pulsed lasers with temporal widths reaching sub-femtosecond timescales have been used to investigate non-stationary states and to follow dynamical processes in real time. In spite of these significant advances, the complexity of many molecular systems, especially those of substantial size, precludes facile identification of even fundamental properties such as the three-dimensional molecular structure. Moreover, the dynamics of such systems remain to a great extent *terra incognita*.

Biological molecules are of special interest; the elucidation of their structure and dynamics is a prerequisite for an understanding of biological function and of biological processes in general. Numerous biological processes are carried out by proteins and carbohydrates (also frequently called glycans, sugars or oligosaccharides), often in their combination as in glycosylated proteins. These classes of biomolecules can form large and complex three-dimensional structures, and their analysis poses a formidable challenge. Over the last decades, much progress has been made, in particular in the analysis of proteins. A key role has been played by mass spectrometry (MS), as it has unparalleled sensitivity reaching down to the femtogram range. MS is therefore widely used for analytical purposes or as a selective detection method in basic research studies. Additionally, MS can be used in conjunction with dissociation experiments to gain structural information. In the case of peptides and proteins, this approach is the method of choice to determine primary structure (i.e. the sequence of amino acids). MS itself is, however, insensitive to the higher order three-dimensional structure of biomolecules and also reaches its limitations in the structural analysis of glycans.

To deduce higher order structures, condensed-phase spectroscopic or scattering techniques are often employed. However, these have a limited sensitivity and therefore require high sample densities, which are frequently not available. X-ray crystallography requires uniform crystals to achieve the high resolution required to distinguish between possible conformations, and important structural information can often remain hidden. Likewise, structures from multidimensional NMR experiments are restricted to solution, are often solvent dependent, and typically give only averaged conformational data.

### 6.1.1 Infrared Spectroscopy

An ideal companion for MS is optical spectroscopy and in particular infrared (IR) spectroscopy, as it can be highly sensitive and provide structural information far beyond what is available from MS alone. As a standalone technique, IR spectroscopy has a long history and is one of the most heavily utilized experimental methodologies for the analysis of molecular structure. In the region between 2800 and 4000  $\text{cm}^{-1}$ , vibrations arising from the stretching motion of hydrogen atoms bound to heavy atoms are found. Upon deuteration, these modes shift to the 2000–2800  $\text{cm}^{-1}$  range. Located between 500 and 2000  $\text{cm}^{-1}$  is the so-called molecular fingerprint region, where the IR-active heavy-atom stretching and many bending modes are found. In the far IR (or THz) region below 500  $\text{cm}^{-1}$ , primarily modes involving very heavy atoms and large-amplitude modes of groups of atoms are present. The exact position of IR bands depends on the details of chemical bonding and the local environment of the IR oscillators. IR spectra can therefore be used to obtain detailed information about the structure and the covalent and non-covalent interactions in molecules.

### 6.1.2 Action Spectroscopy

Most traditional condensed-phase IR spectroscopy experiments are performed by measuring the attenuation that light experiences after passing through a sample. Although this approach is also possible in the gas phase for molecules that have sufficient vapor pressure, it is not generally applicable to many interesting species, including molecular ions, because their attainable densities are many orders of magnitude too low for a measurable light attenuation. For such systems, a different spectroscopic approach can be taken by measuring not *what the molecules do to the light* (as in the aforementioned absorption spectroscopy) but rather *what the light does to the molecules*, thus employing one of several schemes of *action spectroscopy*. Whereas for regular photon absorption measurements, the figure of merit is given by the product  $n * l * \sigma$ , with  $n$  being the number density of the molecules,  $l$  the optical path-length and  $\sigma$  the absorption cross section, the figure of merit for action spectroscopy is given by  $F * \sigma$ , with  $F$  being the photon fluence. Thus, whereas a high number of molecules/ $\text{cm}^2$  ( $n * l$ ) is the requirement in regular absorption measurements, a high number of photons/ $\text{cm}^2$  is necessary in action spectroscopy.

Examples of action spectroscopy include direct measurements of an excited state population via monitoring photon emission or employing techniques to cause photon-induced dissociation or ionization. In a related method, one can also monitor a change in mass of a molecule, complex or cluster that is directly or indirectly caused by the absorption of photons. Using UV light, this change can be caused by direct bond breaking, and when using IR light, the absorbed energy can be redistributed causing thermal dissociation.

### 6.1.3 IR Multiple Photon Dissociation (IRMPD) Action Spectroscopy

IR multiple photon dissociation (IRMPD) spectroscopy of gas-phase ions [1–3] is at present a widely used form of action spectroscopy [4–6]. In IRMPD, the species of interest are exposed to intense IR radiation. When the frequency of the light is resonant with an IR-active transition of the molecule, the sequential absorption of multiple photons can take place. The internal energy of the molecule can then increase to an extent that dissociation takes place. Monitoring the dissociation yield as a function of IR frequency gives the IRMPD spectrum. Over the years, IRMPD has proven to be a versatile and successful technique to record IR spectra of a wide range of species. Examples include biological molecules ranging from amino acids [7] to peptide aggregates and proteins [3, 8, 9], fragmentation products of gas-phase ions [10], species of astrophysical interest [11] and many other molecules and clusters [5, 6].

When considering IRMPD, it is important to distinguish between the sequential absorption of *multiple photons* and a *multiphoton* absorption process within one mode. In the former scenario, which is the relevant one for IRMPD, the timescale between successive absorption events is long compared to the timescale of internal vibrational redistribution (IVR) of the energy. A consequence is that vibrational modes are statistically populated, and hence the ground state of the light-absorbing mode is usually populated. Direct mode anharmonicities therefore play only a minor role. However, the frequencies of the light-absorbing modes are affected by cross-anharmonicities with other low-frequency modes that are statistically populated, giving rise to a dynamical broadening and frequency shift of the absorbing mode. These effects are qualitatively understood, can in some cases be quantitatively modeled [4], and give rise to shifts, broadening and differences between IRMPD and linear IR absorption spectra. These differences can be large when the species involved have very high fragmentation barriers, contain modes with very high anharmonicity, or isomerize during the excitation process. Molecules that are complex with many close-lying IR-active modes often have broad and unstructured room-temperature linear IR absorption spectra, and often multiple conformers are present. Performing IRMPD on such a system yields spectra that are often very congested with a correspondingly low information content. Examples of where IRMPD results in broad spectra include systems where a proton is shared between two functional groups [12]. In these cases, the motion of the proton occurs in an extremely anharmonic potential, causing couplings and spectral congestion, which can be resolved using alternative spectroscopic methods [13].

Many of the complications in IRMPD spectroscopy arise from the IRMPD excitation process itself, and the initial ion temperature (usually room temperature) as such is only a minor issue. Significantly improved spectra can be obtained by performing spectroscopy on ions that are cold and, at the same time, using methods where the absorption of a single, or maybe very few, photons is monitored. One possibility for cooling is to make use of a molecular beam expansion. Ions can then be directly

generated in the source [14] or via resonant photoionization of a molecule-buffer gas cluster [15], and IR absorption is monitored via recording of the IR-induced dissociation. Methods where mass-to-charge selected ions are trapped in a cold ion trap and irradiated by IR light are more versatile, however, and are performed in a number of laboratories [16–19]. Detection of IR absorption can then occur by monitoring IR-induced fragmentation, either of the ion itself or of a weakly bound ion-messenger complex. Typical messengers are rare gas atoms or small molecules such as H<sub>2</sub> or N<sub>2</sub>. For some species, alternatively, the depletion (or enhancement) in yield of a subsequent UV-photodissociation step can be monitored. Using these techniques, many ionic species have been investigated and characterized. However, in many instances, even lower temperatures are desirable, and in addition, the above schemes are difficult to apply to large molecules and ions. In these cases, embedding of the analyte in liquid helium is potentially advantageous and offers exciting new opportunities.

### 6.1.4 Action Spectroscopy Using Helium Nanodroplets

At low temperatures, helium shows behavior unlike any other element or material. Due to strong quantum behavior, bulk liquid helium becomes superfluid at 2.16°K, and helium is the only element that remains liquid down to the absolute zero of temperature. Particles in superfluid helium can move almost freely without any friction. Because helium provides an isothermal environment that interacts only weakly with dopants and is transparent throughout most of the electromagnetic spectrum, it can be regarded as the ultimate cryogenic matrix for spectroscopic investigations.

Experimentally, however, bulk liquid helium is not well suited to “dissolve” molecules, as these would rather aggregate or stick to the container walls. A breakthrough occurred some twenty years ago, when initial experiments were performed in which small, thermally evaporated gas-phase molecules were captured by helium droplets produced via supersonic expansion of low-temperature helium gas into vacuum [20–22]. Using this pickup technique, atoms [23], small molecules [24–27] and biomolecules [28–30] as well as large species such as C<sub>60</sub> [31] have successfully been doped into helium droplets. It was shown that, due to the weak interactions in liquid helium, molecules embedded in helium nanodroplets can rotate almost freely, and their optical spectra show narrow linewidths [24, 27], which evidenced that the helium droplets are indeed superfluid [32]. An analysis of the rotational population distribution revealed the droplet temperature to be only 0.4°K [27]. It has also been observed that in vibrational spectra, line positions are only very weakly affected by the presence of the helium environment [33]. In contrast, electronic spectra of molecules in helium droplets show a rather large influence of the helium on the line positions and general appearance of the spectra, which can be used to extract information on the interaction between the dopant and the helium surrounding [28, 34].

Using laser vaporization, less volatile materials such as refractory metal atoms can be evaporated and picked up by helium droplets [35]. Both techniques, thermal

evaporation as well as laser vaporization, allowed for the growth of clusters inside helium droplets [36, 37]. These clusters occur in a distribution of sizes that is governed by Poisson statistics. Helium droplets are also uniquely suited for studies of the dynamics of dopants inside or on the surface of the droplets [38]. Using pulsed lasers, molecules can be aligned [39], or brought to rotation [40], or their wavepacket dynamics studied [41]. For small molecules, the rotational spectra and dynamics were recently described quantitatively with the help of a new quasi-particle, the angulon [42]. Further, helium droplets have been discussed and used as matrices for electron or X-Ray diffraction experiments [43–45]. Helium nanodroplets can also accommodate charged species. See [46] for a recent review. In such experiments, charged doped droplets can be produced by electron- or photoionization of doped neutral clusters [47], by the pickup of ions by helium droplets [48, 49] or by pickup of neutral species by charged droplets [50].

## 6.2 Experiments on Ions in Helium Nanodroplets

In the following, we describe an experimental setup that has been developed at the Fritz-Haber-Institut (FHI) over the last ten years to measure IR spectra of mass-to-charge selected ions in helium droplets. As the ion-doped droplets carry a charge, their mass-to-charge ratio can be measured using standard techniques. In the first experiments, large droplets were used to capture the mass-to-charge selected protein cytochrome c (molecular weight  $\sim 12,000$  amu) in various charge states, and the droplet size distributions were determined [48]. Later, the first UV/VIS spectroscopic experiments were performed on the hemin ion [51]. After the FHI free-electron laser (FHI FEL) went online, IR action spectroscopy experiments were performed on small molecules [52–54] and clusters [55, 56], peptides and proteins [57, 58], DNA fragments [59], carbohydrates [60–64], reactive intermediates [65–68] and lipids [69, 70]. Here, we show some examples of IR spectroscopy of small anionic complexes as well as of carbohydrate ions in helium droplets.

### 6.2.1 *Pickup of Mass-to-Charge Selected Ions in Helium Droplets*

In most helium droplet experiments, neutral atoms or molecules of interest are brought into the gas phase, picked up by helium droplets, and probed spectroscopically. In typical experiments where a single atom or molecule per droplet is to be picked up, the sample is present in the pickup region at pressures on the order of  $10^{-6}$ – $10^{-3}$  mbar, corresponding to densities of  $\sim 10^{10}$ – $10^{13}$  molecules/cm<sup>3</sup>. This density is limited by the corresponding vapor pressure, which, if needed, can be increased by heating the sample. Of course, all molecules will transform or decompose at a

certain temperature, and for the vast majority of (biologically relevant) molecules, this temperature is much below the hypothetical temperature at which they would have a sufficient vapor pressure to enable helium droplet experiments. Under some circumstances, laser desorption might be a solution, as the heating rate caused by the laser is very high, and (thermal) desorption can occur before decomposition. However, also in this case, at least partial decomposition will occur, and experiments that do not involve mass separation or identification will yield ambiguous results.

A solution is to marry helium droplet methods with modern mass spectrometric techniques that enable the introduction of biological molecules into the gas phase as charged species and to perform mass-to-charge selection. Electrospray ionization (ESI) can be used to bring species ranging from small molecules to large proteins, or even entire viruses, as singly or multiply charged species into the gas phase. Usually, the charge stems from a lack or excess of protons or from complex formation with, for example, alkali cations ( $\text{Na}^+$ ,  $\text{K}^+$  etc.) or halide anions ( $\text{I}^-$ ,  $\text{Br}^-$ ,  $\text{Cl}^-$  or  $\text{F}^-$ ), and the observed charge or charge distribution often reflects the one that the molecule possesses in the condensed phase. Mass spectrometry can then be used to select and isolate an ion in an individual mass-to-charge state, which can then be picked up by a helium droplet.

In the instrument developed at the FHI in Berlin, the pickup of mass-to-charge-selected ions occurs in an ion trap. Conceptually, this is quite analogous to the pickup of neutral molecules in a pickup cell. The general scheme is shown in Fig. 6.1. Shown in (a) is the conventional approach used in many laboratories to capture neutral molecules in a pickup chamber. Depending on the molecule density, the length of the pickup chamber and the size of the helium droplets, a number of molecules can be picked up by the droplets according to a Poisson distribution. The doped droplets can then be interrogated further downstream. The analogous approach for ion pickup is shown in (Fig. 6.1b). In this method, the pickup cell is replaced by a linear ion trap. Mass-to-charge selected ions can be loaded into the trap up to the space charge limit ( $\sim 10^6$  ions/cm<sup>3</sup>). The ions remain stable in the trap for an extended period of time. The droplets traverse the trap and can pick up an ion, and because the kinetic energy of the doped droplet is higher than the trapping potential, the doped droplet can escape the trap and be interrogated further downstream.

An overview of the instrument is shown in Fig. 6.2. The front-end mass spectrometer is a modified commercial mass spectrometer (Waters Q-TOF Ultima). It is equipped with an ESI source (either regular or nano-ESI). The spray usually occurs from an aqueous solution of the molecules of interest into atmospheric pressure. Ions are transferred via several stages of differential pumping into high vacuum. Mass selection is performed with a quadrupole mass spectrometer (mass-to-charge range up to 3000 m/z). In the commercial instrument, this would be followed by a collision cell to induce fragmentation and a high-resolution time-of-flight (TOF) mass spectrometer to analyze the fragments. In our modified instrument, the collision cell is not used, and a quadrupole bender is inserted just in front of the TOF mass spectrometer. This bender allows the ion beam to be sent straight through to be analyzed in the TOF mass spectrometer, or to be deflected 90 degrees and injected into an ion trap. The ion trap is a linear hexapole trap of length 30 cm, and the six

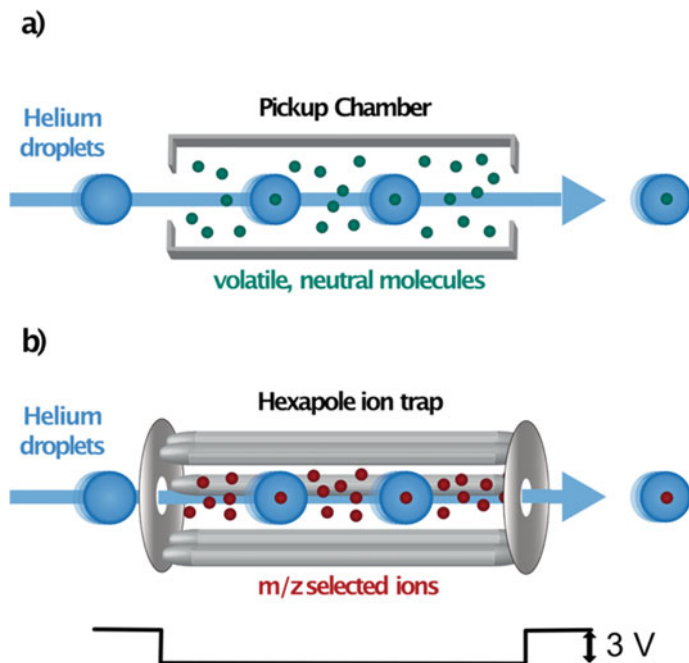


**Fig. 6.1** **a** Pickup of neutral molecules by helium nanodroplets using a pickup chamber in which the molecule of interest is evaporated. This approach is only feasible when the molecule of interest has sufficient vapor pressure. **b** Pickup of ions from an ion trap. The trap can be filled with mass-to-charge selected ions from a mass spectrometer. Longitudinal trapping is achieved by a small trapping potential (1–3 V). The kinetic energy of a doped droplet is more than enough to overcome this trapping potential

rods (5 mm diameter) are mounted with an inscribed circle of 9.1 mm diameter. Alternating phase radio frequency voltage ( $\sim 1$  MHz, 100–300 V p–p) is applied to the six rods, providing for an effective confining potential in the transverse direction. In the longitudinal direction, electrodes at both ends of the trap provide for a shallow (1–3 V) trapping potential. The ions are injected slightly above the trapping potential, and a short pulse of helium gas ( $\sim 10^{-3}$  mbar) is supplied into the trap to allow for removal of the excess kinetic energy such that the ions remain stable in the trap for at least several minutes. The trap temperature can be varied in the range  $\sim 80$ –400 K, and the ions quickly thermalize to that temperature.

The trap is filled up to the space charge limit (on the order of  $10^6$ – $10^7$  ions/cm<sup>3</sup>), which takes, depending on the ion current from the mass spectrometer, from less than one to several seconds. The trap is then traversed by helium droplets.

A pulsed, cryogenic Even-Lavie valve (EL-C-C-2013, Uzi Even & Nachum Lavie, Tel Aviv, Israel) is used to generate helium droplets. The valve-body can be cooled down to 6°K using a closed-cycle helium cryocooler (RDK 408D2, Sumitomo Heavy Industries Ltd., Tokyo, Japan). Combining a resistive heating element with a diode



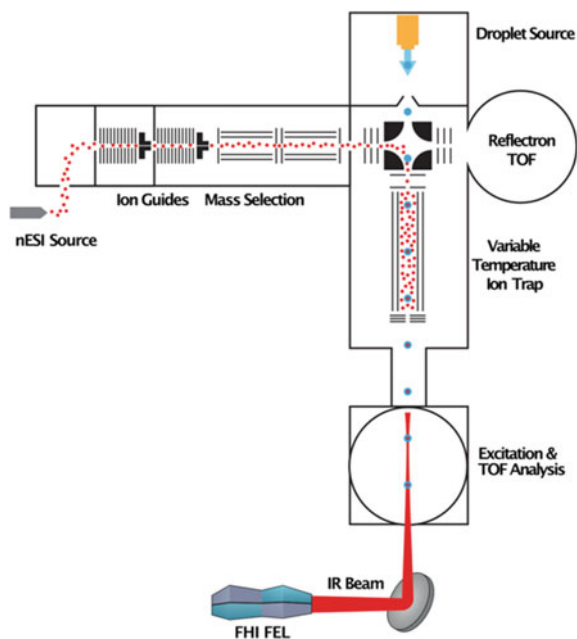


**Fig. 6.2** Schematic overview of the experimental setup. Ions are generated by nano-electrospray ionization (nESI) and transferred into high vacuum by two ion guides. The ions can be monitored by a reflectron time-of-flight (TOF) mass spectrometer. Once the ions of interest are isolated by the quadrupole mass filter and the ion current is optimized, they are injected into the hexapole ion trap. The ion trap is traversed by a beam of helium nanodroplets that can pick up trapped ions and thermalize them to 0.4 K. The helium droplets transport the embedded ions to the detection region where they are irradiated by an IR laser beam produced by the FHI free-electron laser (FHI-FEL) [71]

temperature sensor allows control of the valve temperature, which is typically kept between 15 and 25°K. Controlling the temperature is used to change the size of the helium droplets, and the size distribution can be well described by a log-normal distribution. In the present setup, the mean value of the size distribution can be shifted from around  $10^4$  helium atoms at 25°K to around  $10^6$  helium atoms at 15°K. For experiments presented in this work, the valve was operated at a temperature of 21 or 23°K, a stagnation pressure of 70 bar, and a typical opening time of approximately 10  $\mu$ s. The droplet source vacuum chamber is pumped by a turbomolecular pump with a pumping speed of 2400 l/s (Turbo-V 3°K-T, Agilent Technologies Italia, Italy) maintaining a pressure of  $<10^{-5}$  mbar during operation. The central part of the molecular beam is transmitted towards the hexapole ion trap using a skimmer (Model 50.8, Beam Dynamics, Jacksonville, FL, USA) that has an aperture diameter of 4 mm and is placed around 15 cm away from the nozzle.

In the here presented experiment, the droplets have an average size of  $\sim 5 \cdot 10^4$  helium atoms (and therefore a much larger mass than the ions in the trap) and move at a velocity of  $\sim 500$  m/s. With  $E_{\text{kin}} = 1/2 mv^2$ , the droplets have an average

kinetic energy of  $\sim 520$  eV. When a droplet collides with an ion, its capture can occur, and the then-doped droplet will move with almost unchanged velocity, kinetic energy and direction, compared to the droplet before the collision. As the kinetic energy of the doped droplet is much higher than the longitudinal trapping potential of the ion trap ( $\sim 3$  V), the doped droplets can exit the trap and travel towards the laser interaction region. It is important to note that the ions are otherwise stable in the trap, and the only relevant ion loss channel for the trap is the transport inside a helium droplet. This selective ion confinement makes the method extremely efficient.

Using the present setup, we demonstrated that small ions such as a protonated amino acid as well as large ions such as the protein cytochrome c (molecular weight  $\sim 12,000$  amu) in charge states ranging from  $+6$  to  $+14$  can be efficiently incorporated into helium droplets [48, 51, 57, 58]. Measuring the current from doped droplets with a calibrated amplifier gives peak currents of up to  $\sim 20$  pA, which implies about  $10^4$  ion-doped droplets per pulse. Those intensities are high enough to enable many spectroscopic experiments, as ion-detection schemes can be employed that have sensitivities down to individual ions. Based on the ion density and the droplet sizes, it can be estimated that the probability that a helium droplet picks up an ion is about 2%, ensuring that multiple ion pick-up by a single droplet is negligible.

Because the doped droplets carry charge, they can be manipulated using electric fields. To determine the size distributions, the doped droplets can be accelerated using a static electric field after exiting the trap. As lighter droplets will arrive at earlier times at either a detector or in the laser interaction region, size distributions of the doped droplets can be measured, allowing experiments on droplets with defined sizes to be performed.

## 6.2.2 *The FHI Free-Electron Laser*

Several tens of centimeters downstream of the ion trap, the doped droplet beam is colinearly overlapped with the IR beam of the FHI FEL [71]. To date, a wide range of the electromagnetic spectrum can be covered by various commercially available benchtop laser systems. However, a single laser system often only provides a narrow spectral range with low-intensity radiation. If, on the other hand, high intensity radiation over a broad spectral range is required, an FEL can be the best option. This principle is implemented in the FHI-FEL [71], which is highly tunable and provides intense IR radiation in the range of  $200\text{--}3500$   $\text{cm}^{-1}$ , thus covering the complete molecular fingerprint region as well as much of the light atom stretching region.

The concept of an FEL was proposed in 1971 [72], and the first realization was reported in 1976 [73]. In an IR FEL, a relativistic beam of electrons, produced by an accelerator, is injected into a resonator consisting of two high-reflectivity mirrors at each end of an undulator. The magnetic field in the undulator is perpendicular to the direction of the electron beam and periodically changes polarity a (large) number of times along its length. This causes a periodic deflection, a ‘wiggling’ motion, of the

electrons while traversing the undulator. The transverse motion is quite analogous to the oscillatory motion of electrons in a stationary dipole antenna and hence will result in the emission of radiation with a frequency equal to the oscillation frequency. This oscillation frequency is given by the ratio of the velocity of the electrons to the path length travelled by the electrons per period of the undulator. This path length is larger than the period ( $\lambda_u$ ) of the magnetic field by a factor  $(1 + K^2)$  due to the transverse motion of the electrons induced by the magnetic field; the dimensionless factor  $K$  is a measure of the strength of this magnetic field. The overall motion of the electrons in the undulator resembles the motion of oscillating electrons in a dipole antenna moving close to the speed of light. This high velocity results in a strong Doppler shift: the frequency of the radiation emitted in the forward direction as measured in the laboratory frame is typically up-shifted by a factor  $\sim\gamma^2$ , where  $\gamma$ , the Lorentz factor, is a measure of the electron energy in units of its rest mass. This radiation, referred to as spontaneous emission, is usually very weak. This is a consequence of the fact that the electrons are typically spread out over an interval that is much larger than the radiation wavelength and will therefore not emit coherently. However, on successive round trips in the resonator, this weak radiation will be amplified by fresh electrons, until saturation sets in at a power level that is typically  $10^7$ – $10^8$  times that of the spontaneous emission.

A schematic overview of the FHI-FEL and its main components is shown in Fig. 6.3. The electron beam used to generate the laser beam is produced by an electron gun emitting pulses of free electrons into vacuum. The time structure of the FEL is characterized by a macro- and a micro-repetition rate that also determines the time structure of the laser radiation. The macro-pulse repetition rate is usually set to 10 Hz, and each macro-pulse is 10  $\mu$ s long and consists of  $10^4$  micro-pulses generated at a repetition rate of 1 GHz. After traversing a buncher cavity that compresses the bunch-length, the electrons are accelerated by two linear accelerators (LINACs). The first LINAC accelerates the electrons to a fixed energy of around 20 meV and the second LINAC is used to vary the final electron energy between 18 and 45 meV. Next, the electron beam is directed through a U-shaped bend by dipole and quadrupole magnets before entering the laser cavity. Inside the cavity resides a 2 m long undulator containing 50 periods of oppositely poled NdFeB permanent magnets. The first electron bunch passing through the undulator emits an initial incoherent IR pulse. This optical pulse is reflected by the FEL cavity mirrors and passes through the undulator again. The length of the laser cavity (5.4 m) is set such that the cavity round-trip time of the optical pulse is synchronized with the electron bunches entering the cavity. As a consequence, both pulses travel along the magnetic fields of the undulator, and the electromagnetic field of the radiation can interact with each electron bunch. This interaction leads to micro-bunching of the electrons and the emission of coherent radiation with high intensity gains. The laser output characteristics can be precisely controlled by detuning (shortening) the optical cavity by a multiple of the laser wavelength. A small detuning, such as  $1 \lambda$ , generates short IR pulses with high peak power. Because the spectrum of the radiation is Fourier-limited, these short pulses have a broader spectral width. In this work, the FEL was typically operated

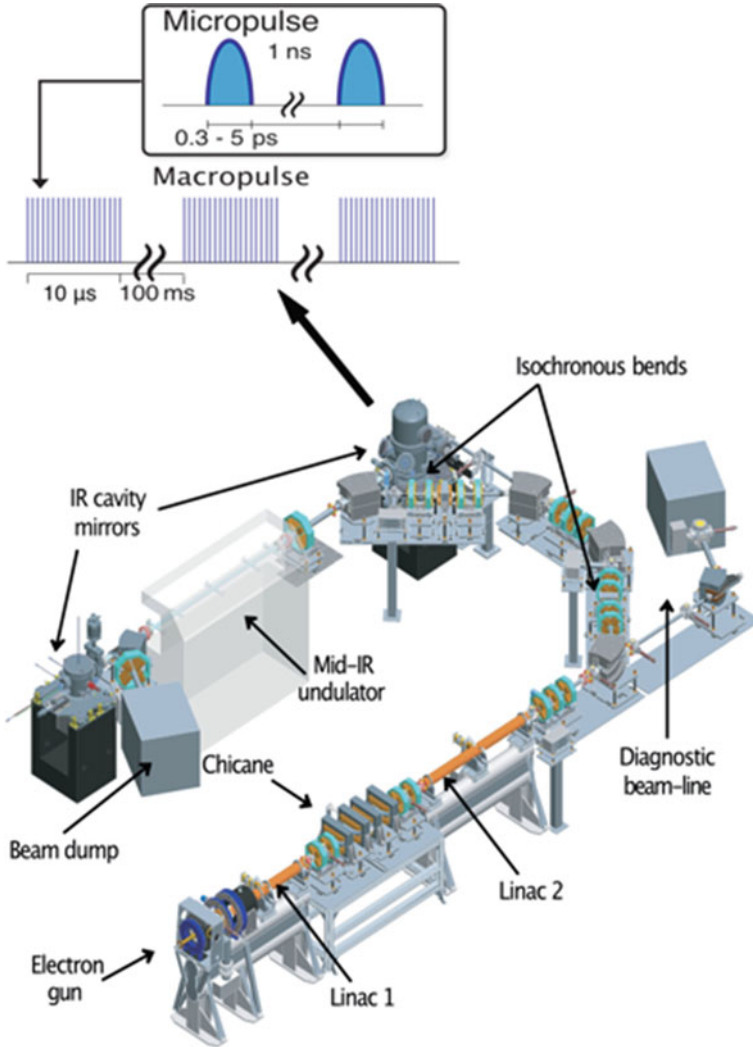


**Fig. 6.3** Schematic overview of the FHI-FEL [71]. An electron gun releases bunches of electrons into vacuum that are accelerated to relativistic velocities by two linear accelerators (LINACs). Inside the laser cavity, a periodic array of strong magnets forces the relativistic electrons on an oscillatory wiggling motion emitting monochromatic radiation. Constructive interference between the electromagnetic field of the radiation and the electrons amplifies the emission of coherent photons

at a detuning of  $3\text{--}5 \lambda$ , which increases the pulse length to a few picoseconds and decreases the spectral width to around 0.2–0.5% (FWHM).

A hole in one of the cavity mirrors is used to transmit a fraction of the radiation to the user experiments and diagnostic elements. During a beam shift (typically one day), the electron energy is kept constant, and the laser wavelength can be tuned by changing the gap between the undulator magnets. The resulting laser radiation has a macro-pulse length of 10  $\mu\text{s}$  and a macro-pulse energy of up to 120 mJ, maintaining a bandwidth of around 0.5% (FWHM). Changing the electron energy allows the FHI-FEL to produce photons with a wavelength between 3 and 60  $\mu\text{m}$ .

### 6.2.3 IR Excitation of Ions in Helium Droplets

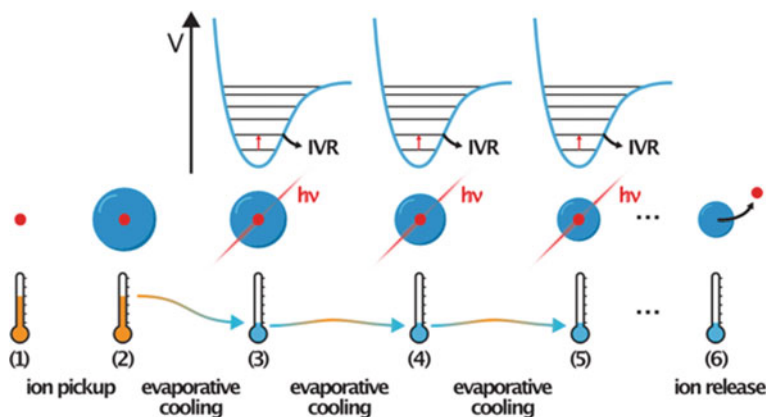
Action spectroscopy can be performed on chromophores embedded in helium droplets. When the doped droplets are irradiated with laser light and when the dopant ion absorbs a photon, an energy relaxation cascade will follow, leading to warm-up of the droplet and finally to the evaporation of helium atoms. The pathways and timescales are generally not known and are topics in our research group. For almost all well-behaved molecules, however, these timescales will be much faster than the timescale at which the next micropulse arrives (1 ns).<sup>1</sup> The following micropulse will then encounter a dopant ion that is cooled down to the droplet equilibrium temperature of 0.4°K and embedded in a slightly smaller droplet. After successive absorption events, bare ions, void of any helium solvation shell, are observed. Some experiments indicate that bare ion generation is the result of the ions being ejected from the droplets [47]; the mechanism for such a process is, however, unclear. Another possibility is that the droplet is completely evaporated. Which of the two processes occurs might depend on the type of ion, the excitation process and other parameters. In any case, the resulting unsolvated ions can be detected in a TOF mass spectrometer. A scheme of the process is shown in Fig. 6.4.

Figure 6.5 shows mass spectra obtained after irradiating helium droplets that are doped with the protonated pentapeptide Tyr-Gly-Gly-Phe-Leu (YGGFL;  $\text{C}_{28}\text{H}_{38}\text{N}_5\text{O}_7^+$ ) at  $1704 \text{ cm}^{-1}$  and different laser macropulse energies. In the mass spectra in Fig. 6.5, essentially only the protonated YGGFL at  $m/z \approx 556$  is observed. At lower mass-to-charge, little to no signal from fragmentation of the peptide is observed. At higher mass-to-charge, no signal of adducts or the remainder of a helium solvation shell can be seen. The signal of the protonated YGGFL increases with increasing laser energy, however not linearly.

Figure 6.6 shows the dependence of the signal intensity on the laser energy for three different droplet size distributions that were selected by accelerating the droplet beam in an electric potential (30 V) and timing the FEL such that the IR light beam

---

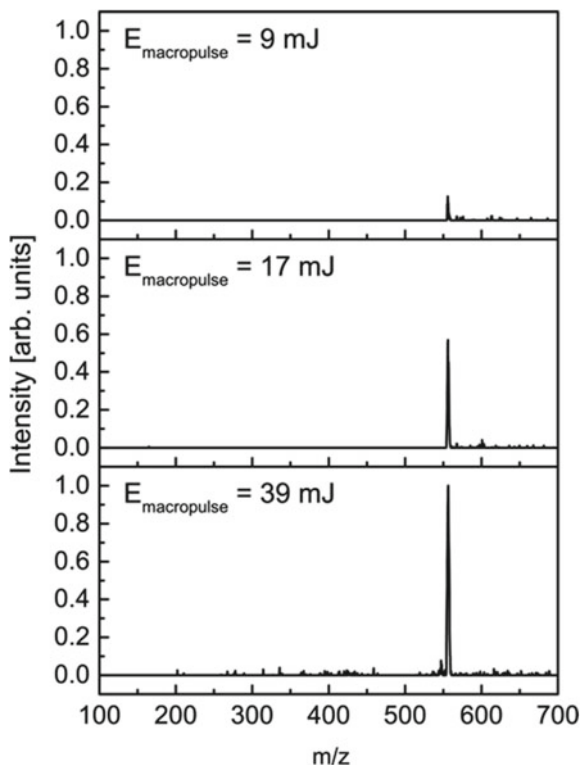
<sup>1</sup> This will be the case for essentially all molecules consisting of more than two atoms. An exception are diatomic molecules with only high frequency vibrational modes, such as HF, for which very long vibrational lifetimes in helium droplets have been observed [74].



**Fig. 6.4** Schematic diagram of the mechanisms involved in IR spectroscopy of ions using helium droplets. The ions inside the hexapole ion trap (1) have an initial energy that is rapidly dissipated after pickup by helium droplets (2) that maintain an equilibrium temperature of 0.4°K by evaporative cooling. The absorption of a resonant photon (3) leads to vibrational excitation of the ion. The absorbed energy is quickly dissipated to the bath of vibrational degrees of freedom by intramolecular vibrational redistribution (IVR). Before the next laser micro-pulse arrives, the ion will return to its vibrational ground state by dissipating its energy to the helium droplet. Evaporation of helium atoms allows the helium droplet to re-thermalize to its equilibrium temperature. This process can repeat itself many times, and after the successive absorption of multiple resonant photons (4) + (5) the bare ion is released from the helium droplet (6). The number of released ions is then monitored as a marker for photon absorption

intersects with the desired droplet size distribution. The corresponding distributions are shown on the left in Fig. 6.3 (a, c, e). They result from simulations, based on experimental data on the time profiles of the entire distribution, measured further downstream in the instrument. The corresponding energy dependence curves on the right (b, d, f) show a clear nonlinear behavior. Whereas in the case of the distributions of the smaller droplets (a, c), signal is already observed for small laser energies, a substantial amount of laser energy is needed for onset of signal in the case of distribution (e). As the absorption of light will occur in different FEL micropulses in a sequential fashion, the number of absorbed photons is directly proportional to the laser energy. If the absorption cross section and the spatial characteristics of the laser beam would be known accurately, the x-axis could be converted from laser energy to number of photons absorbed. Measuring the ion signal at a specific laser energy setting could thus tell us directly how many photons on average are absorbed and therefore serve as an *if, and if so, how many* marker for photon absorption. By monitoring the bare ion yield as a function of wavelength, an IR-action spectrum can be obtained. Importantly, although multiple photons are absorbed, all absorption events will occur from the vibrational ground state of the ion at 0.4°K. Anharmonicities or cross anharmonicities that broaden spectra in IRMPD spectroscopy will therefore not play a role, and narrow absorption bands are expected.

**Fig. 6.5** Mass spectra obtained after irradiating helium droplets doped with the protonated pentapeptide YGGFL at  $1704\text{ cm}^{-1}$  at three different laser energy settings. In all mass spectra, essentially only the intact parent ion at  $m/z \approx 556$  is observed. The signal intensity increases non-linearly with increasing laser energy



As examples, Fig. 6.7 shows experimental spectra of three different species in helium droplets. Shown in (a) is a spectrum of an anionic complex in which a proton holds together two formic acid anions  $(\text{HCO}_2^-)_2 \cdot \text{H}^+$  [52]. Theory predicts that the equilibrium position of the proton is exactly halfway between the two formate ions. Clearly, the spectrum shows several sharp peaks. All of them are very narrow, and their width is determined by the spectral width of the FEL. An analysis of the spectrum shows that all lines in the spectrum below  $1200\text{ cm}^{-1}$  stem from motion of the shared proton coupled to deformation and torsional modes of the complex. Interestingly, the potential in which this proton moves is extremely anharmonic and more closely resembling a particle in a box potential than a harmonic oscillator. Maybe surprisingly, this does not lead to significant broadening. This shared-proton complex and the resulting spectrum can therefore serve as an interesting test case for experiment and theory of our understanding of anharmonic interactions [52].

Shown in (b) is the spectrum of a glycan, a naturally occurring tetrasaccharide, the blood group antigen Lewis b. The type and connectivity of the carbohydrate subunits is shown according to a symbol nomenclature [75]. This nomenclature and the spectroscopy of some carbohydrates will be discussed in more detail in forthcoming pages of this contribution. Considering the size and complexity of the molecule, a surprisingly well-resolved spectrum is obtained. Shown in (c) is the

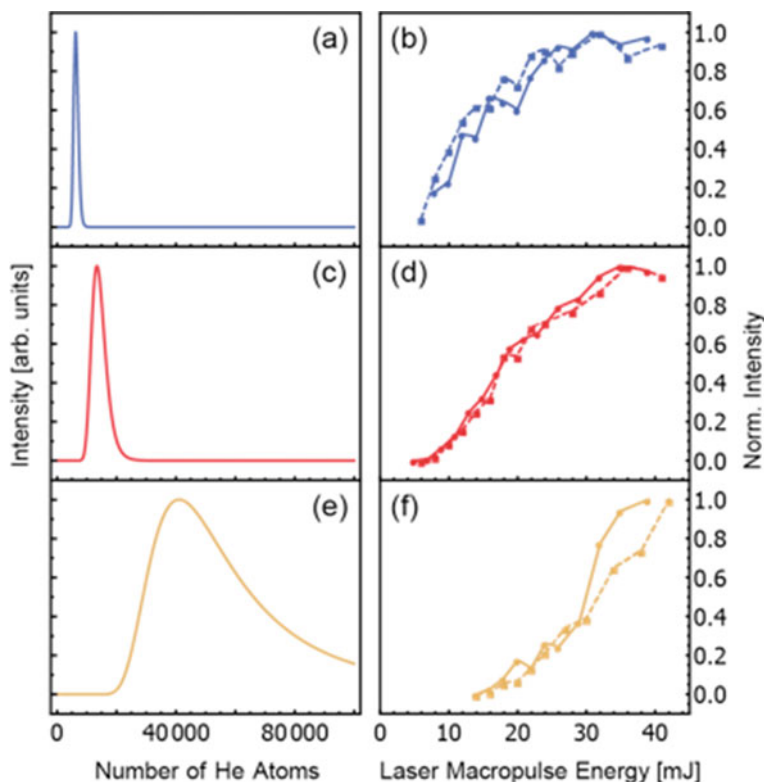
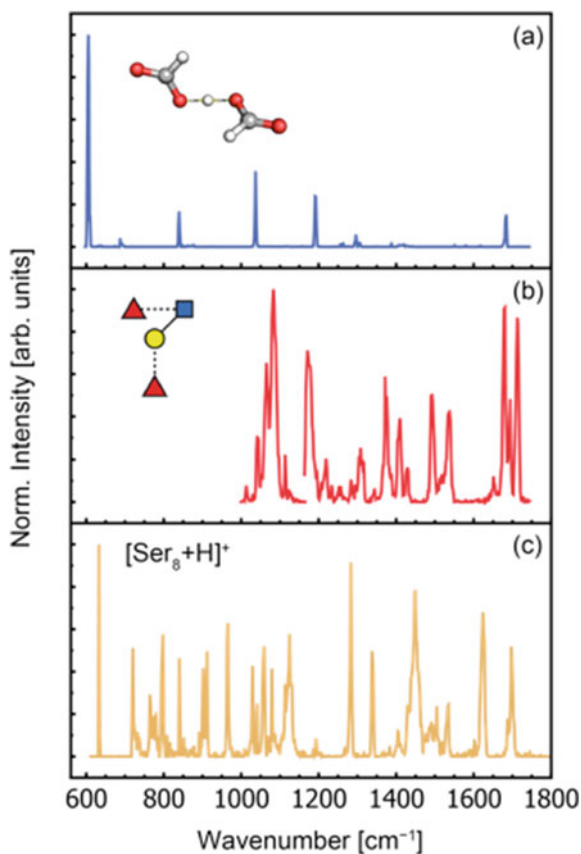


**Fig. 6.6** Droplet size distributions (a, c, e) and signal intensity as a function of laser energy (b, d, f). Clearly, especially for the case of the larger droplets, the signal depends non-linearly on the laser energy and shows a threshold energy. Small droplet sizes are useful for measuring absorption spectra, while larger droplets can be used as a marker for how many photons were absorbed in, for example, IR-IR pump probe experiments

IR spectrum of a non-covalently bound complex consisting of eight amino acids (serine) and one extra proton. This complex has received a great deal of attention, as its high abundance in mass spectrometry experiments indicates a high stability, and further because this complex has a strong preference for homochirality [76, 77]. Its IR spectrum between  $600$  and  $1800\text{ cm}^{-1}$  shows a multitude of sharp resolved bands that are characteristic for the complex and that led, together with other experiments and computation, to a structural assignment [55].



**Fig. 6.7** IR spectra of three species in helium droplets. **a** two formate anions bound by a proton, **b** a naturally occurring tetrasaccharide and **c** a complex containing eight serine molecules and a proton



### 6.3 Spectroscopy of Ions in Helium Droplets: Results on Small Anionic Complexes and Carbohydrates

#### 6.3.1 Fluoride-CO<sub>2</sub>-H<sub>2</sub>O Chemistry

The halide ions I<sup>-</sup>, Br<sup>-</sup>, Cl<sup>-</sup> or F<sup>-</sup> are ubiquitous in nature, and their chemistry is of utmost importance not only in biology, but also in diverse fields such as geochemistry, atmospheric chemistry, and industrial chemistry. Important aspects of their properties include the ability to form strong hydrogen bonds and to participate in nucleophilic substitution reactions. The fluoride ion plays a special role among the halide ions. The high proton affinity and small ionic radius of fluoride promotes the formation of strong ionic hydrogen bonds in the complexation with protic molecules. Furthermore, the fluoride can also act as a potent nucleophile and for example undergo an exothermic reaction with carbon dioxide to yield fluoroformate, FCO<sub>2</sub><sup>-</sup>, forming a covalent bond between F and C. This is of special interest, as the chemistry of CO<sub>2</sub>

and possible ways to remove it from the gas phase are presently very active areas of research. Fluoroformate has been investigated by various experimental techniques, and McMahon and co-workers first generated gas-phase  $\text{FCO}_2^-$  by fluoride ion transfer to study its thermochemistry by ion cyclotron resonance spectroscopy [78, 79]. The experimental findings gave a bond dissociation enthalpy ( $\text{DH}_{298}$ ) of  $133 \pm 8$  kJ/mol, significantly weaker than typical C–F bonds ( $\text{DH}_{298} > 400$  kJ/mol) [80]. Infrared spectra of  $\text{FCO}_2^-$  trapped in an argon matrix were measured, but the presence of multiple species within the matrix hindered band assignment [81]. Later, the tetramethylammonium salt of  $\text{FCO}_2^-$  was isolated and characterized by infrared spectroscopy and solid-state NMR [82]. In addition, photoelectron spectroscopy was used to measure the electronic transitions between  $\text{FCO}_2^-$  and the fluoroformyloxy radical,  $\text{FCO}_2\cdot$  [83]. Furthermore,  $\text{FCO}_2^-$  as well as other halide ion– $\text{CO}_2$  complexes have been investigated by ab initio calculations [84–86].

We have explored the chemistry of  $\text{F}^-$  with  $\text{CO}_2$  and  $\text{H}_2\text{O}$  by applying mass spectrometry coupled to infrared spectroscopy of ions in liquid helium droplets and ab-initio molecular dynamics simulations [53, 54]. In the experiment, a few  $\mu\text{L}$  of an aqueous solution of sodium fluoride ( $\text{NaF}$ ) at a concentration of 1 mM/L is placed into a nESI capillary. The solution is sprayed into atmosphere to which additional  $\text{CO}_2$  gas is added to increase the  $\text{CO}_2$  level to a few % (the exact amount has not been quantified), and the instrument is set to transmit and detect anions. To aid in the assignment of molecular composition and to facilitate the assignment of IR spectra, deuteration experiments are also performed. To do so, the  $\text{NaF}$  is dissolved in  $\text{D}_2\text{O}$ , and the  $\text{CO}_2$  is bubbled through  $\text{D}_2\text{O}$  before being brought to the ESI region. Ions are then transferred into the instrument, and mass spectra are recorded using the on-axis TOF mass spectrometer.

Figure 6.8 shows a mass spectrum of the ions obtained. The spectrum is surprisingly simple, consisting of three dominant peaks. At the lowest  $m/z = 61$ , a peak corresponding to the bicarbonate anion is observed, and at  $m/z = 63$ , the  $\text{FCO}_2^-$  ion is found. Interestingly, the most intense peak in the mass spectrum occurs 18  $m/z$

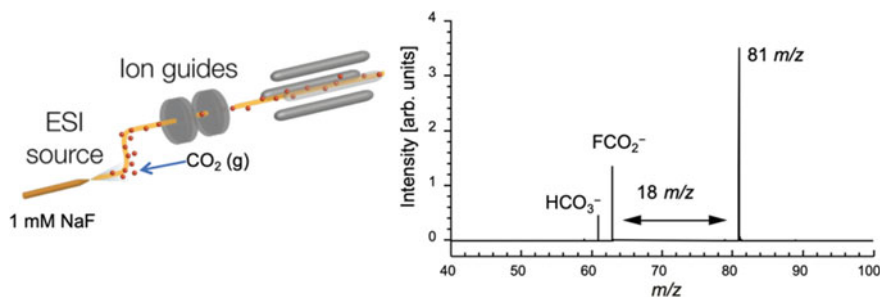


**Fig. 6.8** A 1 mM aqueous  $\text{NaF}$  solution is sprayed via nESI into air, to which some  $\text{CO}_2$  gas is added. Anions are then transferred into the vacuum of the instrument and mass spectra are recorded (right side). The mass spectrum consists of three intense peaks, which can be assigned to  $\text{HCO}_3^-$ ,  $\text{FCO}_2^-$  and the adduct or reaction product of  $\text{FCO}_2^- + \text{H}_2\text{O}$ . The ions can then be captured in helium droplets and investigate via IR spectroscopy

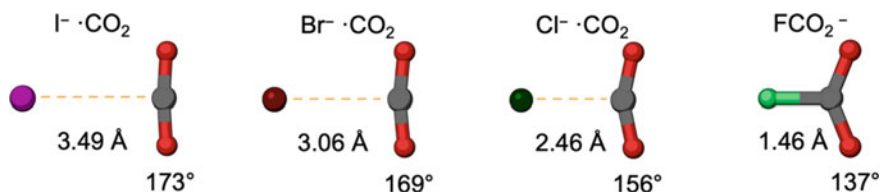


**Fig. 6.9** Calculated structures of halide ion—CO<sub>2</sub> complexes at the MP2/def2-TZVPP level. The initial structures for X = I<sup>-</sup>–Cl<sup>-</sup> are taken from [86]

higher than (presumably) FCO<sub>2</sub><sup>-</sup>, indicating the addition of one water molecule to FCO<sub>2</sub><sup>-</sup>. The observation of the strong FCO<sub>2</sub><sup>-</sup> was somewhat surprising; the fact that FCO<sub>2</sub><sup>-</sup> is a stable ion was known, however, its facile production in the ESI process had not been reported. When replacing NaF by NaCl, no signal corresponding to ClCO<sub>2</sub><sup>-</sup> is observed, nor is signal indicating an ion 18 m/z larger observed.

Figure 6.9 shows structures calculated at the MP2/def2-TZVPP level for X·CO<sub>2</sub> complexes (X = I<sup>-</sup>, Br<sup>-</sup>, Cl<sup>-</sup> and F<sup>-</sup>) (X = I<sup>-</sup>–Cl<sup>-</sup> from [86]; X = F<sup>-</sup> this work). It can be seen that for I<sup>-</sup>–Cl<sup>-</sup>, the halide-carbon distance remains larger than is common for a covalent bond, however also that the O–C–O angle decreases, indicative of at least some electron donation from the halide ion into antibonding O–C–O orbitals. The situation is different for FCO<sub>2</sub><sup>-</sup>, for which both the structure (Fig. 6.9) as well as energetics [78, 79] indicate a stronger covalent character of the F–C bond and significant electron donation into the CO<sub>2</sub> moiety.

The FCO<sub>2</sub><sup>-</sup> ion can be incorporated into helium droplets, and the IR spectrum can be recorded, as shown in Fig. 6.10, middle trace. For comparison, the IR-spectrum of the well-known formate ion HCO<sub>2</sub><sup>-</sup> in helium droplets has been measured in the 1200–1800 cm<sup>-1</sup> range (top trace). This spectrum shows two very narrow peaks at 1317 and 1623 cm<sup>-1</sup> stemming from the symmetric and antisymmetric O–C–O stretching motion in HCO<sub>2</sub><sup>-</sup>, respectively. These measurements compare very well to literature values of 1314 and 1622 cm<sup>-1</sup> for those modes [87]. It therefore seems that the helium environment does not induce a strong shift (at least no more than estimated 1–5 cm<sup>-1</sup>) in line positions. Another striking observation concerns the width of the bands. In the spectra of both the formate and fluorofomate anions, the bands are very narrow, exhibiting full width at half maximum (fwhm) widths between 2 and 6 cm<sup>-1</sup>. This is in some instances narrower than the spectral width of the FHI-FEL (typical fwhm of ~0.5% of the photon energy). Most likely, this is caused by the non-linear nature of the dependence of the observed bare ion signal on laser fluence.

Shown in the middle trace of Fig. 6.10 is the helium droplet IR spectrum of the fluorofomate anion, and a total of six bands can be observed. For some of them, facile assignment based on previous experiments is possible [81, 82]. At 548 cm<sup>-1</sup>, a band that can be assigned to result from C–F stretching motion is observed. This value is significantly red-shifted from the value of a typical C–F bond (>1000 cm<sup>-1</sup>) due to the weakness of the C–F bond in FCO<sub>2</sub><sup>-</sup>. The transition at 747 cm<sup>-1</sup> can be assigned to result from O–C–O bending motion (δ(OCO)). At around 1270 cm<sup>-1</sup>, only one

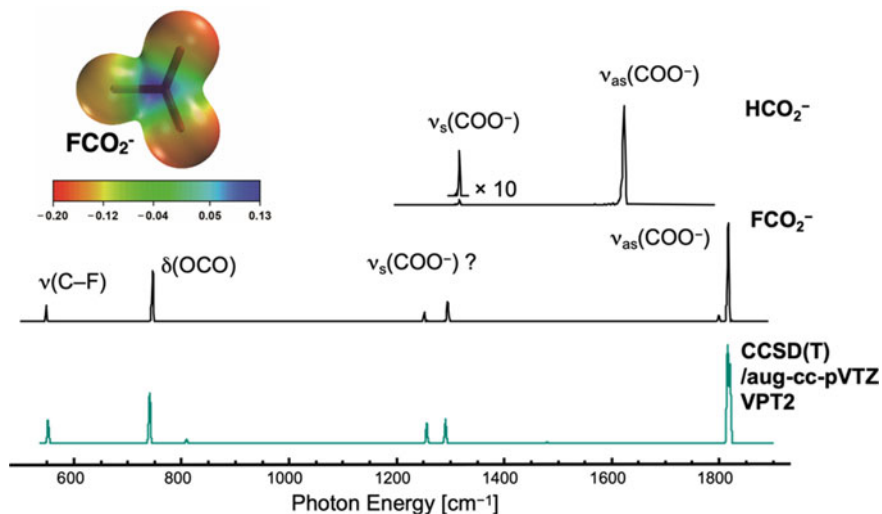


**Fig. 6.10** Vibrational spectrum of (a) formate and (b) fluoroformate obtained using the helium nanodroplet method. Shown in (c) is the theoretical vibrational spectrum of fluoroformate with anharmonic corrections calculated utilizing the VPT2 method at the CCSD(T)/aug-cc-pVTZ level of theory. Excellent agreement is observed between the experimental and theoretical vibrational spectra of fluoroformate, most notably for the Fermi resonance between  $\nu_s(\text{COO}^-)$  and  $\nu(\text{C-F}) + \delta(\text{OCO})$ . However, theory overestimates the degree of vibrational wave function mixing in the Fermi resonance between  $\nu_{\text{as}}(\text{COO}^-)$  and  $\delta(\text{C-F}) + \nu_s(\text{COO}^-)$ . The top right corner shows the calculated electrostatic potential around the  $\text{FCO}_2^-$  anion. It can be seen that the negative charge is distributed among the F- and O-atoms, with a slightly higher negative charge on the O-atoms

band resulting from symmetric O–C–O stretching motion ( $\nu_s(\text{COO}^-)$ ) is expected, whereas the experiment shows two bands, one at  $1251\text{ cm}^{-1}$  and one at  $1294\text{ cm}^{-1}$ . Similarly, only one band, stemming from antisymmetric O–C–O stretching motion ( $\nu_{\text{as}}(\text{COO}^-)$ ) is expected to the blue, whereas the experiment shows two bands, a weak band at  $1799\text{ cm}^{-1}$  and a stronger band at  $1816\text{ cm}^{-1}$ .

A complete assignment of the spectrum can be performed with the help of quantum chemistry. The ion is small enough for the “gold standard” method in quantum chemistry, coupled cluster with single, double and perturbative triple excitations (CCSD(T)) in combination with the rather large aug-cc-pVTZ basis set, to be applied. Calculations of vibrational frequencies are in most cases performed using the harmonic approximation. Here, we go beyond that and include anharmonicities, overtones, combination bands and Fermi resonances using the VPT2 method [88–90], as implemented within CFOUR [91]. Shown in the lower trace of Fig. 6.10 is the result of those calculations. The calculated line positions and intensities are convoluted with an 0.5% (full width at half maximum) gaussian function. No scaling of the horizontal axis has been applied. It can be observed that the calculations reproduce the experiment extremely well. The results from theory can also be used to elucidate the nature of the two doublets around  $1270$  and  $1800\text{ cm}^{-1}$ . It turns out that the doublet near  $1270\text{ cm}^{-1}$  is caused by a Fermi resonance between the combination

mode  $\nu(\text{C-F}) + \delta(\text{OCO})$  with  $\nu_s(\text{COO}^-)$ . Near  $1800 \text{ cm}^{-1}$ , theory also predicts two bands, however with much less splitting and almost equal intensity which stems from a Fermi interaction of  $\nu_s(\text{COO}^-) + \delta(\text{C-F})$  with  $\nu_{\text{as}}(\text{COO}^-)$ . The prediction for this Fermi interaction is less accurate, most likely as the theoretical description of the  $\delta(\text{C-F})$  mode is poorer [53].

An interesting question is the nature of the ion that occurs at  $m/z = 81$  in Fig. 6.8 and gives rise to the most intense peak. Typically, the intensity is directly related to the stability and further, as the ion is generated in in the ESI process in moist air, it must be largely unreactive towards at least oxygen, water or  $\text{CO}_2$ . The species with  $m/z = 81$  is exactly 18  $m/z$  higher in mass than  $\text{FCO}_2^-$ , indicating that it is either an adduct or reaction product of  $\text{FCO}_2^-$  with  $\text{H}_2\text{O}$ .

To elucidate the structure of the  $m/z = 81$  ion, we recorded its IR spectrum in helium droplets and performed calculations of possible  $\text{FCO}_2^- + \text{H}_2\text{O}$  adducts or reaction products [54]. The results are shown in Fig. 6.11, with the experimental spectrum shown in the top trace. Candidate structures were optimized using the MP2 method using the aug-cc-pVTZ basis set, anharmonic IR spectra were calculating using the GVPT2 method [92, 93] as implemented in Gaussian 16 [94]. When comparing the experimental spectrum to the results of the calculations, it is clear

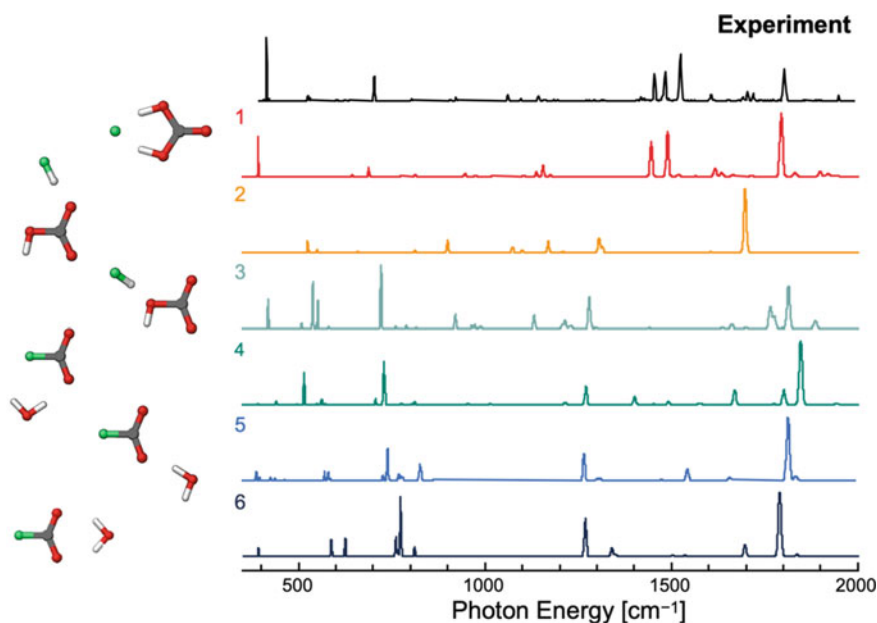


**Fig. 6.11** Experimental infrared spectrum of the  $[\text{H}_2\text{CO}_3\text{F}]^-$  species compared to theoretical spectra of candidate structures. The experimental spectrum (black) was collected by ion infrared action spectroscopy in helium nanodroplets. Theoretical spectra for candidate structures 1–6 were calculated at the MP2/aug-cc-pVTZ level of theory with anharmonic corrections from the GVPT2 method. The experimental spectrum matches best to the spectrum calculated for structure 1

that the best match of the experimental spectrum is to the spectrum of structure **1**—a complex of carbonic acid with  $F^-$  [54].

The generation of a stable complex between carbonic acid and fluoride is highly intriguing. Carbonic acid is central to many chemical processes, yet it is thermodynamically unstable, undergoing decomposition to yield carbon dioxide and water. Although the barrier to dissociation is large for an isolated carbonic acid molecule, the dissociation reaction is catalyzed by complexation with many abundant molecular species, most notably water, ammonia, formic and acetic acid, and other carbonic acid molecules, which renders experimental characterization very challenging. The observed  $H_2CO_3 + F^-$  complex is extremely stable and observed as the most abundant ion produced in the electrospray process under the employed conditions, providing a robust chemical trap for the normally elusive carbonic acid molecule. Complexation with anions and isolation in helium droplets was proven to be a successful method to further examine the structure and properties of this elusive molecule.

### 6.3.2 *Carbohydrates*

Among the four major classes of biomolecules in mammals—DNA, RNA, proteins and carbohydrates—carbohydrates remain the most poorly characterized. Carbohydrates are synonymously termed glycans, oligo- or polysaccharides or also in a broader sense simply sugars. Historically, carbohydrates were exclusively linked to functions such as energy storage, bioscaffolds, or cellular decorations in the absence of identified biological functions. In our everyday life, carbohydrates play a role as sources of nutrition, but carbohydrates are in fact a manifold class of biomolecules. The following pages present an introduction to some of the important functions of carbohydrates relevant to mammalian biology.

In biochemistry and medicine, the sequencing of the human genome was a breakthrough to the elucidation of all template-driven processes that derive from the identified genes. RNA and protein research advanced at incomparable speed. Glycosylation patterns, however, cannot be directly linked to the template of the human genome. Furthermore, many glycosylation patterns are not rigid but highly dynamic over time, which is obvious in an evolutionary sense, but accounts for physiological variations as well as pathological variations. The diverse roles of carbohydrates span from inflammation via cell adhesion to molecular recognition and cell–cell interactions [95–99]. To name an example of outstanding interest throughout the past year, the dense glycosylation on the outer shell of the spike proteins of coronaviruses shields the viruses from antibody recognition, enabling them to evade the host's immune response. In addition, some coronavirus glycosylation sites have a structural role relevant for host cell entry [100–103].

Formerly, carbohydrates, or the hydrates of carbons, were represented by the empirical formula  $C_n(H_2O)_m$ . As known today, many naturally occurring carbohydrates are exceptions from the empirical formula, for example deoxyhexoses or

*N*-acetylhexoses, the latter of which is depicted in Fig. 6.12. The chemical representation in Fig. 6.12 is typically used in the wider field of organic chemistry and known as a skeletal formula. Carbon and hydrogen atoms are only implicitly depicted or excluded for clarity reasons. All heteroatoms and the hydrogen atoms attached to these are explicitly depicted. Using wedged bonds, the chair conformation classically used for six-membered rings is illustrated in a three-dimensional way. To minimize steric repulsion between functional groups, monosaccharides in heterocyclic ring forms are not planar but puckered [104]. Besides the chair conformation, the families of conformations are boat, envelope, half-chair and skew. For simplicity, the chair conformation is most often used in illustrations.

The most basic units in carbohydrates are monosaccharides. Generally, monosaccharides can be present in an open chain form or in two different heterocyclic ring forms. Five-membered rings are called furanoses and the usually preferred six-membered rings pyranoses, see Fig. 6.12. Monosaccharides are grouped by the number of carbon atoms into tetroses, pentoses, hexoses or heptoses, containing four, five, six and seven carbon atoms, respectively. These groups are further divided by the functional groups present in open chain form, such as aldoses with an aldehyde or ketoses with a ketone functional group. Each group comprises a number of possible monosaccharides, isomers, that differ in the orientation of the hydroxyl groups, or in mentioned exceptions the orientation of other functional groups. Monosaccharides that differ in only one stereocenter are called epimers. The carbon atoms in a monosaccharide are labelled numerically, i.e. in the heterocyclic ring form counting clockwise from the ring oxygen beginning with the carbon atom at C1 position. The D- or L configuration is defined by the orientation of the hydroxyl group at the stereocenter furthest from the highest oxidized carbon atom in open chain form, or in the heterocyclic ring form at the carbon atom in the ring furthest from C1. The stereocenter at C1, termed anomeric center, is created with the ring-closing reaction. The two possible configurations are termed alpha ( $\alpha$ ) and beta ( $\beta$ ) anomers, according to the relative orientation at the anomeric center and the highest, chiral carbon atom in the ring, the anomeric reference atom. In aqueous solution,  $\alpha$ - and  $\beta$ -anomers can interconvert into each other in a process called mutarotation.

Going to larger carbohydrates, disaccharides are composed of two monosaccharides and oligo- or polysaccharides are polymers of larger numbers of monosaccharides. Monosaccharides, which define the composition of carbohydrates, are connected covalently via glycosidic linkages. In a condensation reaction, the glycosidic linkage is formed between the hydroxyl group at the anomeric center and one

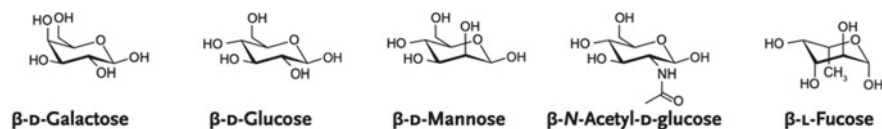


**Fig. 6.12** Examples for prominent monosaccharides in mammals. All monosaccharides are aldohexoses adopting a pyranose ring structure

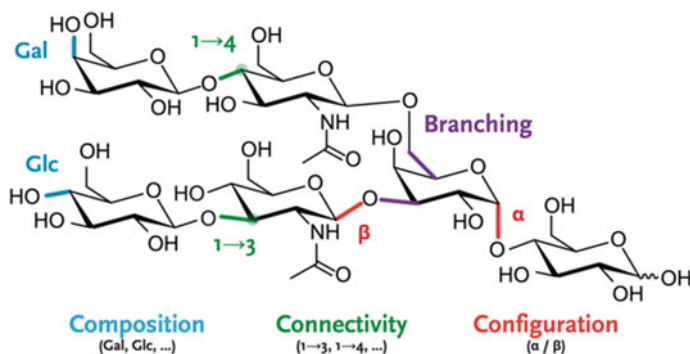


**Fig. 6.13** A generic glycan illustrating the structural details of glycans: branching, composition, connectivity and configuration. The composition of a glycan is defined by the monosaccharides present. The connectivity, in locked  $\alpha$ - or  $\beta$ -configuration, indicates which hydroxyl group are involved in the glycosidic linkage. Branching is possible in larger carbohydrates

of the hydroxyl groups of the other monosaccharide, generating  $1 \rightarrow 2$ ,  $1 \rightarrow 3$ ,  $1 \rightarrow 4$  or  $1 \rightarrow 6$  linkages, as illustrated in Fig. 6.13. The formation of a glycosidic bond locks the anomeric center in either the  $\alpha$ - or  $\beta$ -configuration. In contrast to DNA, RNA or proteins, oligo- and polysaccharides are not only linear molecules but can be branched, leading to significant challenges in glycan structural analysis.

Many representations of carbohydrates, such as the Fischer or Haworth projection, evolved to ease the reading of the chemical structures of carbohydrates. For example, for monosaccharides in their open chain form, the Fischer projection is typically used. The symbol nomenclature for glycans (SNFG) is the most commonly used structural representation in the field of carbohydrate chemistry [75, 105]. Figure 6.14b shows a carbohydrate composed of six monosaccharide units in its skeletal formula and

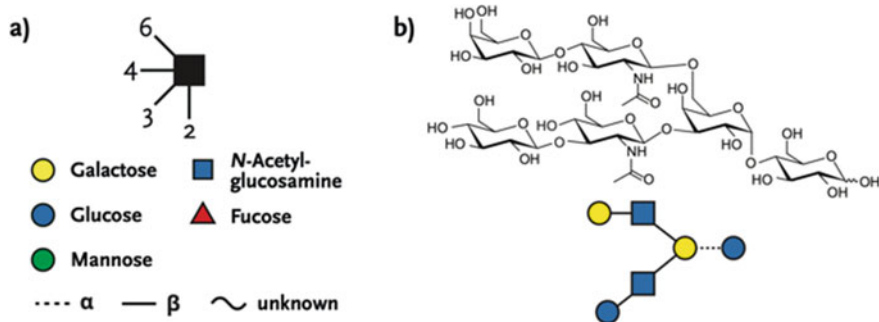


**Fig. 6.14** **a** The symbol nomenclature for glycans (SNFG) [75, 105] is commonly used to illustrate glycan structures. Monosaccharides are represented in colored symbols. A glycosidic linkage is either a dashed or solid line indicating the configuration. The angle of the connecting line shows the connectivity. **b** A generic glycan structure in chemical representation and translated to SNFG



translated to the SNFG nomenclature. The composition of monosaccharides is visualized using colored symbols of different shapes, the connectivity is depicted with the angle of the connecting line at the symbol, and the configuration is represented with either a dashed or a solid line. The standardized use of symbols for monosaccharide building blocks is especially helpful in the depiction of larger structures.

The structural diversity and complexity of carbohydrates is thus very large, yet minute changes can alter the biological function. To address the question if, and in how far IR spectroscopy is sensitive to variations in carbohydrate structure, vibrational spectra of glycans in helium nanodroplets were recorded. Glycan ions are brought into the gas phase by nano-electrospray ionization (nESI). These ions are mass-to-charge selected and accumulated inside the ion trap. Helium nanodroplets with an average size of  $10^5$  helium atoms traverse the trap and can pick up ions and rapidly cool them to the equilibrium temperature of the droplet. Inside the detection chamber, the embedded ions are investigated using laser radiation produced by the FHI-FEL. The subsequent absorption of resonant photons can lead to the release of the bare ion from the droplet, which is used as a marker for photon absorption. Plotting the yield of released ions as a function of laser wavelength yields a highly reproducible IR spectrum. Each spectrum shown here consists of at least two independent scans recorded with a wavenumber step-size of  $\Delta\nu = 2 \text{ cm}^{-1}$ . Although the yield of released ions scales non-linearly with laser energy, a linear correction has been performed by dividing the signal intensity by the laser energy. As a result, relative intensities can be distorted to some extent. The spectra shown here were recorded between  $950$  and  $1700 \text{ cm}^{-1}$  with two different photon fluxes using a variable focusing mirror. A softer focus (lower photon fluence) was used between  $950$  and  $1200 \text{ cm}^{-1}$ . To access the absorption bands between  $1150$  and  $1700 \text{ cm}^{-1}$ , a separate spectrum with a tighter focus (higher photon fluence) was recorded.

To assess the potential of cryogenic ion spectroscopy to resolve the minute structural details present in complex carbohydrates, a series of well-defined amino-alkyl linked carbohydrates as well as natural samples were analyzed. The analyzed samples consist of monosaccharides **1–5**, disaccharides **6–7**, trisaccharides **8–13**, and naturally occurring tetrasaccharides **14–17**, as shown in Fig. 6.15.

### 6.3.3 Mono- and Disaccharides

As discussed in the preceding section, different monosaccharides often share the same mass and only differ in the stereochemistry at single carbon atoms. Using cryogenic ion spectroscopy in helium droplets, IR spectra of the protonated aminoalkyl-linked monosaccharides were recorded (Fig. 6.16). Because the primary amine of the linker has the largest basicity, it will most likely accept a proton upon ionization and provide a localized charge.

The IR spectrum of  $\alpha$ -mannose (**1**) shows a variety of absorption bands. Around  $1150 \text{ cm}^{-1}$ , two narrow and well-resolved absorption bands are found. Preliminary quantum chemical calculations indicate that the most intense bands in this

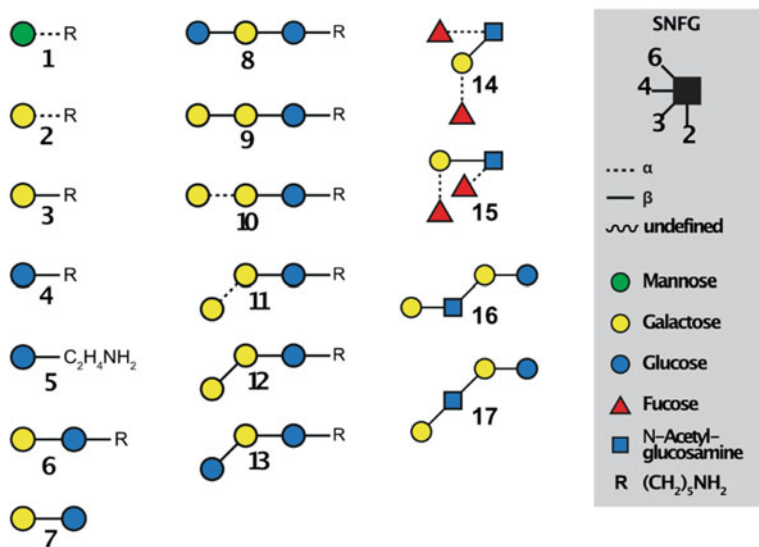


**Fig. 6.15** Schematic SNFG representation of the here investigated molecules. The sets consist of monosaccharides **1–5**, disaccharides **6** and **7**, trisaccharides **8–13**, and biologically relevant tetrasaccharides **14–17**

region ( $1000\text{--}1150\text{ cm}^{-1}$ ) arise from C–O-stretching vibrations with strong transition dipole moments. Between  $1150$  and  $1400\text{ cm}^{-1}$ , additional bands that likely originate from O–H-bend modes are present. Above  $1400\text{ cm}^{-1}$ , a series of partially resolved bands are obtained. According to calculations, these bands correspond to the primary ammonium group of the linker. Interestingly, only three  $\text{NH}_3^+$ -bending modes are expected in this region. The presence of multiple, partially unresolved bands indicates that  $\alpha$ -mannose adopts multiple coexisting conformers with different IR fingerprints in the gas phase. Moving to the isomeric  $\alpha$ -galactose (**2**), the stereoconfiguration at C2 and C4 is inverted. The IR spectrum also shows a variety of resolved absorption bands, but the peak positions and intensities render it distinct from the spectrum obtained for  $\alpha$ -mannose. Again, the presence of multiple absorption bands above  $1400\text{ cm}^{-1}$  indicates multiple coexisting conformers. The IR spectrum of the epimeric  $\beta$ -galactose (**3**) is characterized by several highly resolved absorption bands between  $950$  and  $1400\text{ cm}^{-1}$  and broader absorptions above  $1400\text{ cm}^{-1}$ . Interestingly, some bands are as narrow as the bandwidth of the IR laser radiation (FWHM around  $4\text{ cm}^{-1}$ ). Also, the IR spectrum of  $\beta$ -glucose (**4**) exhibits a number of highly resolved absorption bands up to  $1150\text{ cm}^{-1}$ . Between  $1150$  and  $1500\text{ cm}^{-1}$ , only a few weaker absorptions are present. To examine the influence of the attached aminopentyl linker,  $\beta$ -glucose with a shorter aminoethyl linker (**5**) was investigated. A direct comparison shows that the two spectra are distinct. The spectrum of **5** exhibits fewer absorption bands than the one obtained for **4**, and the peak positions do not coincide. In contrast to the vibrational spectra of monosaccharides **1–4**, only one strong and three weak resolved bands appear above  $1400\text{ cm}^{-1}$ . This

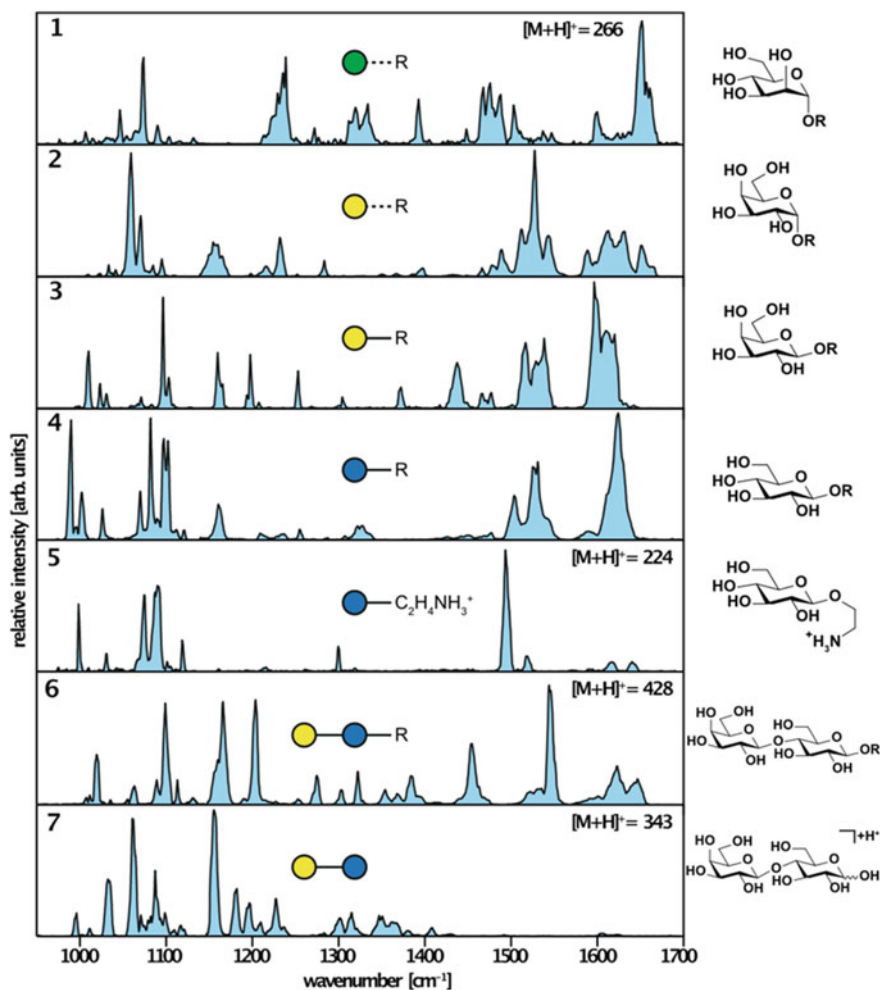


**Fig. 6.16** IR spectra of aminoalkyl-linked monosaccharides **1–7** as well as free (**7**) and aminoalkyl-linked lactose (**6**) investigated as  $[M + H]^+$  ions

could indicate that the gas-phase structure of **5** mainly adopts a single conformer, which could be caused by the reduced flexibility of the shorter linker.

Upon moving to disaccharides, which consist of two monosaccharide building blocks joined by a glycosidic bond, the structural complexity increases significantly. The glycosidic bond can be formed at different hydroxy groups (connectivity isomers) with either an  $\alpha$ - or  $\beta$ -configuration. The increasing system size and the torsional angle of the glycosidic bond further increase the conformational complexity. Although an additional building block is present, the IR spectrum of  $\beta$ -lactose (**6**) shows a similar appearance to the monosaccharides described above. The variety of highly resolved bands provide a unique diagnostic pattern. To further investigate

the influence of the aminoalkyl linker, a spectrum of protonated free lactose (**7**) was recorded. Here, the reducing end does not contain any linker, and the anomeric center can adopt either an  $\alpha$ - or  $\beta$ -configuration. In addition, the location of the charge is uncertain, and different protomers may coexist. Nonetheless, the IR spectrum of **7** exhibits multiple well-resolved absorption bands between 950 and 1400  $\text{cm}^{-1}$ . There are no obvious similarities between the vibrational signatures of both lactose variants, which indicates that their gas-phase structures are widely different. These structural differences most likely result from interactions between the charged linker and hydroxy groups of the disaccharide, or from a distinct charge distribution in **7**. The absence of characteristic absorption bands above 1400  $\text{cm}^{-1}$  confirms the assumption that this region is mainly governed by vibrational transitions of the charged aminoalkyl linker.

### 6.3.4 Trisaccharides

Next, a set of six isomeric trisaccharides was used to benchmark the method. The structures of trisaccharides **8–13** share the same reducing-end  $\beta$ -lactose core-motif and an aminopentyl linker, as shown in Fig. 6.17. The terminal building block was systematically varied to generate isomers that differ in composition, connectivity or configuration. For example, the glycan pairs **8/9** and **12/13** are compositional isomers and only differ in the identity of the terminal building block (Glc vs. Gal). Glycan pairs **9/10** and **11/12** are configurational isomers and differ in the stereoconfiguration of the glycosidic bond. Finally, glycan pairs **8/13**, **9/12** and **10/11** are connectivity isomers that only differ in the position of the glycosidic bond ( $1 \rightarrow 3$  vs.  $1 \rightarrow 4$ ).

These isomeric trisaccharides are extremely difficult to distinguish using established LC–MS techniques. Recent studies [106] used ion mobility-mass spectrometry to approach this analytical challenge and measured the arrival-time distributions and collision cross sections of trisaccharides **8–13**. In negative ion mode, connectivity and configurational isomers were efficiently separated with baseline separation, allowing an unambiguous identification. The remarkable baseline separation also enabled a quantitative analysis of coexisting isomers inside a mixture. However, compositional isomers consistently showed very similar arrival time distributions and could therefore not be distinguished using IM-MS.

The IR spectra of trisaccharides **8–13** are shown in Fig. 6.18. In general, each spectrum exhibits a large number of highly resolved absorption bands and no significant spectral congestion. The configurational isomers **9/10** and **11/12** share the same connectivity and configuration, but differ in the configuration of the terminal glycosidic bond ( $\alpha/\beta$ ). The distinctness of the absorption patterns allows facile differentiation of these conformational isomers. Similar results are obtained for connectivity isomers **8/13**, **9/12** and **10/11**, which exhibit either a  $1 \rightarrow 3$  or  $1 \rightarrow 4$  terminal glycosidic bond. Again, the highly resolved optical signatures reveal differences that allow an unambiguous identification of each connectivity isomer. Most striking are the observations for compositional isomers **8/9** and **12/13**, which share the same

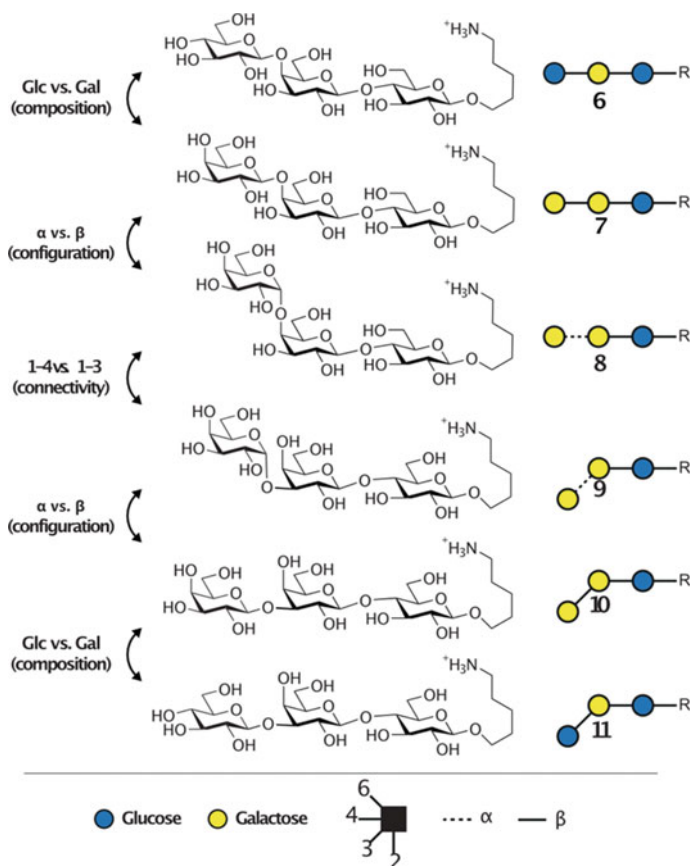


**Fig. 6.17** The synthetic trisaccharides **8–13** only differ in the connectivity (1  $\rightarrow$  3 vs. 1  $\rightarrow$  4), configuration ( $\alpha$  vs.  $\beta$ ), or composition (Glc vs. Gal) of the terminal building block. These isomeric oligosaccharides are extremely difficult to distinguish using established methods and therefore serve as a benchmark for this experimental approach

connectivity and configuration and only differ in the identity of the terminal building block (Glc vs. Gal). In other words, the trisaccharide structures within each isomeric pair only differ in the stereochemical orientation of a *single* hydroxy group. Surprisingly, these minute structural variations lead to substantial differences in the IR signatures, especially above  $1300\text{ cm}^{-1}$ . For example, a characteristic high-intensity transition is observed at  $1450\text{ cm}^{-1}$  for trisaccharide **9**, but is absent in the spectrum of the corresponding compositional isomer **8**. Also, trisaccharide **12** features a strong absorption band around  $1310\text{ cm}^{-1}$  that is absent in the spectrum of the trisaccharide **13**. Taken together, each of the six trisaccharide isomers exhibits a variety of resolved absorption bands that lead to a unique IR signature and allow their unambiguous identification. Similarly to the previously discussed mono- and disaccharides, it is interesting to note that some IR spectra feature more than three absorption bands

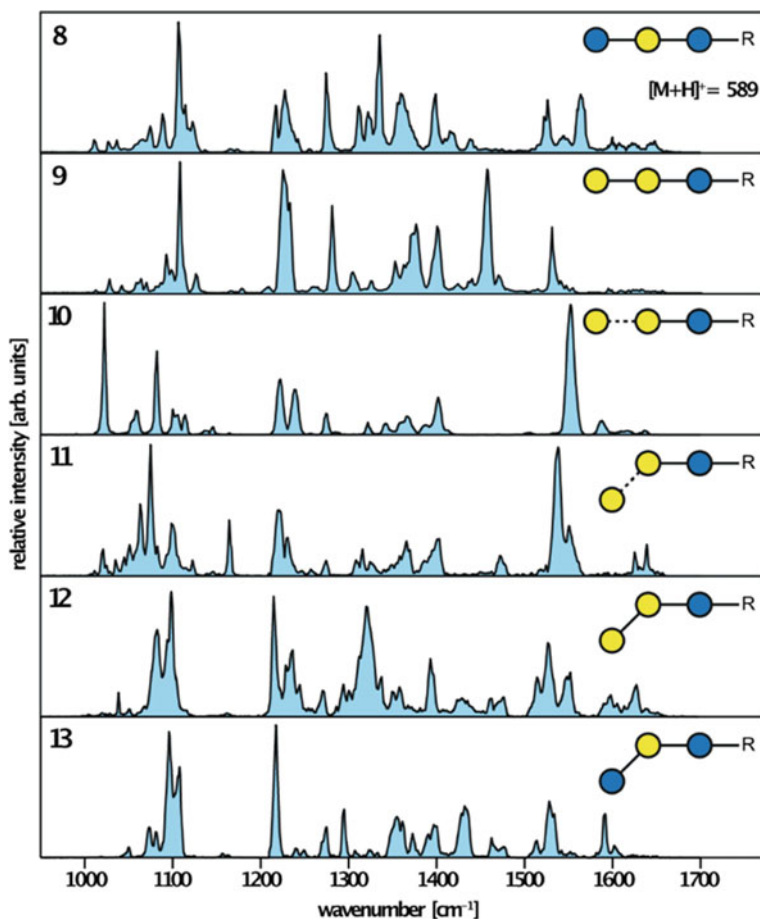


**Fig. 6.18** IR spectra of the isomeric trisaccharides **8–13**. Despite the marginal structural differences between these species, each trisaccharide can be readily distinguished by its unique absorption pattern that contains a variety of resolved bands

expected for the charged aminopentyl linker. For example, trisaccharide **12** features five resolved bands, which indicates the presence of multiple coexisting conformers. Other trisaccharides such as **10** show a much cleaner spectrum with a few absorption bands that are as narrow as the bandwidth of the laser radiation.

### 6.3.5 Naturally Occurring Tetrasaccharides

To extend the scope of this method from synthetic standards to naturally occurring glycans, the blood-group antigens Lewis b ( $\text{Le}^b$ , **14**) and Lewis y ( $\text{Le}^y$ , **15**)

were investigated as sodium adducts. Although it is in principle possible to generate protonated species of these samples, the high salt concentrations found in many samples typically lead to strong signals of sodium adducts. The isomeric tetrasaccharides each consist of an *N*-acetylglucosamine, a galactose and two fucose building blocks and differ in their glycosidic linkages. Similarly to free lactose **7**, the absence of a linker leads to an undefined anomeric center that can adopt either an  $\alpha$ - or  $\beta$ -configuration. Although the number of expected vibrational transitions for molecules of this size is large, the corresponding IR spectra (Fig. 6.19) exhibit a remarkably small number of well-resolved absorption bands that allow an unambiguous discrimination between the two isomeric species. Especially the  $\text{Le}^y$  tetrasaccharide shows an extremely clean IR spectrum with a total of eight features. The transitions around  $1500\text{ m}^{-1}$  and  $1680\text{ cm}^{-1}$  likely stem from the amide group of the GlcNAc building block and are assigned as amide II and amide I bands, respectively. A single amide group is expected to give only one amide II and one amide I band. Here, however,

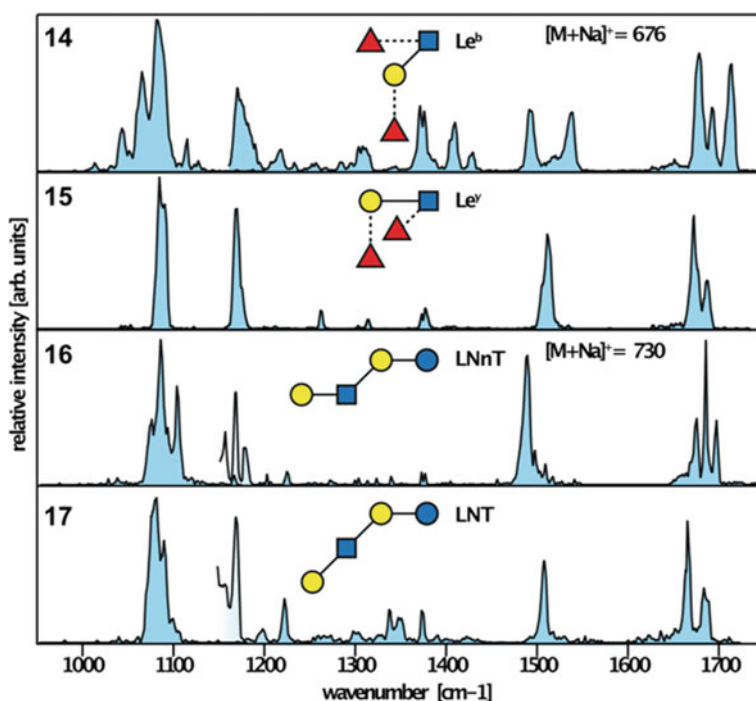


**Fig. 6.19** As representatives of biologically relevant glycans, the blood-group antigens  $\text{Le}^b$  (**14**) and  $\text{Le}^y$  (**15**), as well as the milk-sugar tetrasaccharides lacto-*N*-neotetraose (**16**) and lacto-*N*-tetraose (**17**) were investigated as  $[\text{M} + \text{Na}]^+$  ions. The characteristic absorption patterns allow unambiguous discrimination between the corresponding isomers. The discontinuity in intensity around  $1150\text{ cm}^{-1}$  results from differences in photon fluence in the irradiation region prior to ion detection

multiple bands are observed, which indicates that multiple coexisting conformers with different amide band positions coexist in the gas phase.

As another example for naturally occurring glycans, lacto-*N*-neotetraose (**16**) and lacto-*N*-tetraose (**17**) were investigated. These isomeric tetrasaccharides belong to the group of human milk oligosaccharides and only differ in the connectivity of the terminal galactose building block. The corresponding IR spectra of the sodium adducts shown in Fig. 6.19 also exhibit distinct and well-resolved absorption features that allow their discrimination. Again, multiple bands in the amide II and amide I region indicate the presence of coexisting conformers.

The highly resolved IR spectra allow an unambiguous identification of complex isomeric glycans. But what are the underlying structures that lead to those absorption patterns? In general, theoretical methods are widely used to compute structural candidates and calculate their corresponding IR spectra. These theoretical IR spectra are then compared to experimental results in order to extract the structural information that is encoded in the vibrational fingerprint, and identify the underlying structure. For the glycans presented here, this approach turned out to be challenging. There is a threefold problem: (1) the molecules are extremely flexible, have many rotatable bonds and ring-pucker possibilities, giving rise to a very large conformational space; (2) the molecules are large, and accurate calculations of the structure and energies of individual conformers are very expensive; and (3) calculations of IR spectra beyond the harmonic approximations are presently out of the question for molecules of that size. It turns out that problem (1) is the most severe. For other systems such as peptides and proteins, a pre-screening of the conformational space using a less costly method, such as a simple empirical force field, is often performed. In order to be able to do so, these force fields need to have a certain minimum accuracy to give results that are meaningful for our experiments. For peptides and proteins, such force fields have been developed over several decades and are readily available. For glycans, however, no sufficiently accurate force fields are presently available. A firm conformational assignment of the here investigated molecules therefore requires improvements in the theoretical description.

Nonetheless, cryogenic vibrational spectroscopy is a valuable addition to the structural analysis toolbox for glycans. The low temperature environment of superfluid helium nanodroplets enables the acquisition of highly resolved absorption spectra: a true spectral fingerprint that is unique for each glycan. Even minute structural differences such as the stereochemical orientation of a single hydroxy group within trisaccharides lead to spectral differences that allow an unambiguous identification which is otherwise difficult or impossible to do. The method in general therefore offers possibilities for commercial application in the glycosciences. However, the sophisticated experimental setup used in this work involving a FEL will arguably not find a commercial application. This will be left to simpler implementations using cryogenic ion trap and commercially available benchtop laser systems.



## 6.4 Conclusions

Helium nanodroplets are indeed the ultimate cryogenic matrix for optical spectroscopy experiments. The method can not only be applied to volatile neutral species, but also to a wide variety of anionic or cationic gas-phase ions. When used in combination with mass spectrometric techniques, unprecedented selectivity and sensitivity can be obtained, allowing for the investigation of small ionic complexes, larger biological molecules and even entire proteins, containing thousands of atoms.

The IR spectra shown here are highly diagnostic for the species investigated. For small ions, rigorous theory can quantitatively explain the observations. For larger species, IR spectroscopy in helium nanodroplets can be used as an orthogonal technique to mass spectrometry and ion mobility spectrometry to fingerprint and distinguish molecular isomers or conformers which are indistinguishable by traditional bioanalytic methods. Present and future applications therefore range from fundamental studies on the structure and dynamics of molecules to real world applications in analytical chemistry.

**Acknowledgements** The authors thank the FHI-FEL staff, particularly Sandy Gewinner and Wieland Schöllkopf, for laser operation. D.A.T. gratefully acknowledges the support of the Alexander von Humboldt Foundation.

## References

1. L.I. Yeh, M. Okumura, J.D. Myers, J.M. Price, Y.T. Lee, Vibrational spectroscopy of the hydrated hydronium cluster ions  $\text{H}_3\text{O}^+ \cdot (\text{H}_2\text{O})_n$  ( $n=1, 2, 3$ ). *J. Chem. Phys.* **91**(12), 7319–7330 (1989)
2. H. Oh, K. Breuker, S.K. Sze, Y. Ge, B.K. Carpenter, F.W. McLafferty, Secondary and tertiary structures of gaseous protein ions characterized by electron capture dissociation mass spectrometry and photofragment spectroscopy. *Proc. Natl. Acad. Sci. USA* **99**(25), 15863–15868 (2002). <https://doi.org/10.1073/pnas.212643599>
3. J. Oomens, N. Polfer, D.T. Moore, L. van der Meer, A.G. Marshall, J.R. Eyler, G. Meijer, G. von Helden, Charge-state resolved mid-infrared spectroscopy of a gas-phase protein. *Phys. Chem. Chem. Phys.* **7**(7), 1345–1348 (2005). <https://doi.org/10.1039/b502322j>
4. J. Oomens, B.G. Sartakov, G. Meijer, G. von Helden, Gas-phase infrared multiple photon dissociation spectroscopy of mass-selected molecular ions. *Int. J. Mass. Spectrom.* **254**(1–2), 1–19 (2006). <https://doi.org/10.1016/j.ijms.2006.05.009>
5. N.C. Polfer, J. Oomens, Vibrational spectroscopy of bare and solvated ionic complexes of biological relevance. *Mass. Spectrom. Rev.* **28**(3), 468–494 (2009). <https://doi.org/10.1002/mas.20215>
6. N.C. Polfer, Infrared multiple photon dissociation spectroscopy of trapped ions. *Chem. Soc. Rev.* **40**(5), 2211–2221 (2011). <https://doi.org/10.1039/c0cs00171f>
7. N.C. Polfer, B. Paizs, L.C. Snoek, I. Compagnon, S. Suhai, G. Meijer, G. von Helden, J. Oomens, Infrared fingerprint spectroscopy and theoretical studies of potassium ion tagged amino acids and peptides in the gas phase. *J. Am. Chem. Soc.* **127**(23), 8571–8579 (2005). <https://doi.org/10.1021/ja050858u>

8. H.B. Oh, C. Lin, H.Y. Hwang, H. Zhai, K. Breuker, V. Zabravskov, B.K. Carpenter, F.W. McLafferty, Infrared photodissociation spectroscopy of electrosprayed ions in a Fourier transform mass spectrometer. *J. Am. Chem. Soc.* **127**(11), 4076–4083 (2005). <https://doi.org/10.1021/ja040136n>
9. J. Seo, W. Hoffmann, S. Warnke, X. Huang, S. Gewinner, W. Schöllkopf, M.T. Bowers, G. von Helden, K. Pagel, An infrared spectroscopy approach to follow beta-sheet formation in peptide amyloid assemblies. *Nat. Chem.* **9**(1), 39–44 (2017). <https://doi.org/10.1038/nchem.2615>
10. N.C. Polfer, J. Oomens, S. Suhai, B. Paizs, Infrared spectroscopy and theoretical studies on gas-phase protonated leu-enkephalin and its fragments: direct experimental evidence for the mobile proton. *J. Am. Chem. Soc.* **129**(18), 5887–5897 (2007). <https://doi.org/10.1021/ja068014d>
11. J. Oomens, B.G. Sartakov, A.G.G.M. Tielens, G. Meijer, G. von Helden, Gas-phase infrared spectrum of the coronene cation. *Astrophys. J.* **560**(1), L99–L103 (2001). <https://doi.org/10.1086/324170>
12. D.T. Moore, J. Oomens, L. van der Meer, G. von Helden, G. Meijer, J. Valle, A.G. Marshall, J.R. Eyler, Probing the vibrations of shared, OH<sup>+</sup>O-bound protons in the gas phase. *ChemPhysChem.* **5**(5), 740–743 (2004). <https://doi.org/10.1002/cphc.200400062>
13. J.A. Fournier, C.J. Johnson, C.T. Wolke, G.H. Weddle, A.B. Wolk, M.A. Johnson, Vibrational spectral signature of the proton defect in the three-dimensional H<sup>+</sup>(H<sub>2</sub>O)<sub>21</sub> cluster. *Science* **344**(6187), 1009–1012 (2014). <https://doi.org/10.1126/science.1253788>
14. M.A. Duncan, Frontiers in the spectroscopy of mass-selected molecular ions. *Int. J. Mass. Spectrom.* **200**(1–3), 545–569 (2000). [https://doi.org/10.1016/S1387-3806\(00\)00366-3](https://doi.org/10.1016/S1387-3806(00)00366-3)
15. H. Piest, G. von Helden, G. Meijer, Infrared spectroscopy of jet-cooled neutral and ionized aniline-Ar. *J. Chem. Phys.* **110**(4), 2010–2015 (1999). <https://doi.org/10.1063/1.477866>
16. K.R. Asmis, M. Brummer, C. Kaposta, G. Santambrogio, G. von Helden, G. Meijer, K. Rademann, L. Wöste, Mass-selected infrared photodissociation spectroscopy of V<sub>4</sub>O<sub>10</sub><sup>+</sup>. *Phys. Chem. Chem. Phys.* **4**(7), 1101–1104 (2002). <https://doi.org/10.1039/b111056j>
17. T.R. Rizzo, J.A. Stearns, O.V. Boyarkin, Spectroscopic studies of cold, gas-phase biomolecular ions. *Int. Rev. Phys. Chem.* **28**(3), 481–515 (2009). <https://doi.org/10.1080/01442350903069931>
18. A.B. Wolk, C.M. Leavitt, E. Garand, M.A. Johnson, Cryogenic ion chemistry and spectroscopy. *Acc. Chem. Res.* **47**(1), 202–210 (2014). <https://doi.org/10.1021/ar400125a>
19. J.G. Redwine, Z.A. Davis, N.L. Burke, R.A. Oglesbee, S.A. McLuckey, T.S. Zwier, A novel ion trap based tandem mass spectrometer for the spectroscopic study of cold gas phase polyatomic ions. *Int. J. Mass. Spectrom.* **348**, 9–14 (2013). <https://doi.org/10.1016/j.ijms.2013.04.002>
20. J.P. Toennies, A.F. Vilesov, Superfluid helium droplets: a uniquely cold nanomatrix for molecules and molecular complexes. *Angew. Chem-Int. Edit.* **43**(20), 2622–2648 (2004). <https://doi.org/10.1002/anie.200300611>
21. F. Stienkemeier, K.K. Lehmann, Spectroscopy and dynamics in helium nanodroplets. *J. Phys. B-At. Mol. Opt. Phys.* **39**(8), R127–R166 (2006). <https://doi.org/10.1088/0953-4075/39/8/R01>
22. M.Y. Choi, G.E. Doublerly, T.M. Falconer, W.K. Lewis, C.M. Lindsay, J.M. Merritt, P.L. Stiles, R.E. Miller, Infrared spectroscopy of helium nanodroplets: novel methods for physics and chemistry. *Int. Rev. Phys. Chem.* **25**(1–2), 15–75 (2006). <https://doi.org/10.1080/01442350600625092>
23. F. Stienkemeier, J. Higgins, W. Ernst, G. Scoles, Laser spectroscopy of alkali-doped helium clusters. *Phys. Rev. Lett.* **74**(18), 3592–3595 (1995). <https://doi.org/10.1103/PhysRevLett.74.3592>
24. S. Goyal, D.L. Schutt, G. Scoles, Vibrational spectroscopy of sulfur-hexafluoride attached to helium clusters. *Phys. Rev. Lett.* **69**(6), 933–936 (1992). <https://doi.org/10.1103/PhysRevLett.69.933>
25. R. Fröchtenicht, J.P. Toennies, A. Vilesov, High-resolution infrared-spectroscopy of SF<sub>6</sub> embedded in He clusters. *Chem. Phys. Lett.* **229**(1–2), 1–7 (1994). [https://doi.org/10.1016/0009-2614\(94\)01026-9](https://doi.org/10.1016/0009-2614(94)01026-9)

26. S. Grebenev, M. Hartmann, M. Havenith, B. Sartakov, J.P. Toennies, A.F. Vilesov, The rotational spectrum of single OCS molecules in liquid  $^4\text{He}$  droplets. *J. Chem. Phys.* **112**(10), 4485–4495 (2000). <https://doi.org/10.1021/cr00031a009>
27. M. Hartmann, R. Miller, J. Toennies, A. Vilesov, Rotationally resolved spectroscopy of  $\text{SF}_6$  in liquid-helium clusters—a molecular probe of cluster temperature. *Phys. Rev. Lett.* **75**(8), 1566–1569 (1995). <https://doi.org/10.1103/PhysRevLett.75.1566>
28. A. Lindinger, J. Toennies, A. Vilesov, High resolution vibronic spectra of the amino acids tryptophan and tyrosine in 0.38 K cold helium droplets. *J. Chem. Phys.* **110**(3), 1429–1436 (1999). <https://doi.org/10.1063/1.478018>
29. S. Denifl, F. Zappa, I. Mahr, J. Lecointre, M. Probst, T.D. Mark, P. Scheier, Mass spectrometric investigation of anions formed upon free electron attachment to nucleobase molecules and clusters embedded in superfluid helium droplets. *Phys. Rev. Lett.* **97**(4), 043201 (2006). <https://doi.org/10.1103/PhysRevLett.97.043201>
30. S. Smolarek, A.M. Rijs, W.J. Buma, M. Drabbel, Absorption spectroscopy of adenine, 9-methyladenine, and 2-aminopurine in helium nanodroplets. *Phys. Chem. Chem. Phys.* **12**(48), 15600–15606 (2010). <https://doi.org/10.1039/c0cp00746c>
31. J. Close, F. Federmann, K. Hoffmann, N. Quaas, Absorption spectroscopy of  $\text{C}_{60}$  molecules isolated in helium droplets. *Chem. Phys. Lett.* **276**, 393–398 (1997)
32. S. Grebenev, J.P. Toennies, A.F. Vilesov, Superfluidity within a small helium-4 cluster: the microscopic andronikashvili experiment. *Science* **279**(5359), 2083–2086 (1998). <https://doi.org/10.1126/science.279.5359.2083>
33. K. Nauta, R.E. Miller, Solvent mediated vibrational relaxation: superfluid helium droplet spectroscopy of HCN dimer. *J. Chem. Phys.* **111**(8), 3426–3433 (1999). <https://doi.org/10.1063/1.479627>
34. A. Slenczka, B. Dick, M. Hartmann, J. Toennies, Inhomogeneous broadening of the zero phonon line of phthalocyanine in superfluid helium droplets. *J. Chem. Phys.* **115**(22), 10199–10205 (2001). <https://doi.org/10.1063/1.1409353>
35. P. Claas, S.O. Mende, F. Stienkemeier, Characterization of laser ablation as a means for doping helium nanodroplets. *Rev. Sci. Instrum.* **74**(9), 4071–4076 (2003). <https://doi.org/10.1063/1.1602943>
36. M. Hartmann, R. Miller, J. Toennies, A. Vilesov, High-resolution molecular spectroscopy of van der waals clusters in liquid helium droplets. *Science* **272**, 1631–1634 (1996). <https://doi.org/10.1126/science.272.5268.1631>
37. T. Döppner, T. Fennel, T. Diederich, J. Tiggesbäumker, K.H. Meiwes-Broer KH, Controlling the Coulomb explosion of silver clusters by femtosecond dual-pulse laser excitation. *Phys. Rev. Lett.* **94**(1), 013401(2005) <https://doi.org/10.1103/PhysRevA.61.033201>
38. M.P. Ziemkiewicz, D.M. Neumark, O. Gessner, Ultrafast electronic dynamics in helium nanodroplets. *Int. Rev. Phys. Chem.* **34**(2), 239–267 (2015). <https://doi.org/10.1080/014235x.2015.1051353>
39. D. Pentlehner, J.H. Nielsen, A. Slenczka, K. Mølmer, H. Stapelfeldt, Impulsive laser induced alignment of molecules dissolved in helium nanodroplets. *Phys. Rev. Lett.* **110**(9), 093002 (2013). <https://doi.org/10.1103/PhysRevLett.86.4447>
40. B. Shepperson, A.A. Søndergaard, L. Christiansen, J. Kaczmarczyk, R.E. Zillich, M. Lemeshko, H. Stapelfeldt, Laser-induced rotation of iodine molecules in helium nanodroplets: revivals and breaking free. *Phys. Rev. Lett.* **118**(20), 203203 (2017). <https://doi.org/10.1103/PhysRevLett.118.203203>
41. M. Schlesinger, M. Mudrich, F. Stienkemeier, W.T. Strunz, Dissipative vibrational wave packet dynamics of alkali dimers attached to helium nanodroplets. *Chem. Phys. Lett.* **490**(4–6), 245–248 (2010). <https://doi.org/10.1016/j.cplett.2010.03.060>
42. M. Lemeshko, Quasiparticle approach to molecules interacting with quantum solvents. *Phys. Rev. Lett.* **118**(9), 095301 (2017). <https://doi.org/10.1103/PhysRevLett.118.095301>
43. O. Gessner, A.F. Vilesov, Imaging quantum vortices in superfluid helium droplets, in *Annual Review of Physical Chemistry*, vol. 70, ed. by M.A. Johnson, T.J. Martinez, (2019), pp. 173–198. <https://doi.org/10.1146/annurev-physchem-042018-052744>

44. L.F. Gomez, K.R. Ferguson, J.P. Cryan, C. Bacellar, R.M.P. Tanyag, C. Jones, S. Schorb, D. Anielski, A. Belkacem, C. Bernando, R. Boll, J. Bozek, S. Carron, G. Chen, T. Delmas, L. Englert, S.W. Epp, B. Erk, L. Foucar, R. Hartmann, A. Hexemer, M. Huth, J. Kwok, S.R. Leone, J.H.S. Ma, F. Maia, E. Malmerberg, S. Marchesini, D.M. Neumark, B. Poon, J. Prell, D. Rolles, B. Rudek, A. Rudenko, M. Seifrid, K.R. Siefertmann, F.P. Sturm, M. Swiggers, J. Ullrich, F. Weise, P. Zwart, C. Bostedt, O. Gessner, A.F. Vilesov, Shapes and vorticities of superfluid helium nanodroplets. *Science* **345**(6199), 906–909 (2014). <https://doi.org/10.1126/science.1252395>
45. Y.T. He, J. Zhang, W. Kong, Electron diffraction of CBr<sub>4</sub> in superfluid helium droplets: a step towards single molecule diffraction. *J. Chem. Phys.* **145**(3) (2016). <https://doi.org/10.1063/1.4958931>
46. T. Gonzalez-Lezana, O. Echt, M. Gatchell, M. Bartolomei, J. Campos-Martinez, P. Scheier, Solvation of ions in helium. *Int. Rev. Phys. Chem.* **39**(4), 465–516 (2020). <https://doi.org/10.1080/0144235x.2020.1794585>
47. S. Smolarek, N.B. Brauer, W.J. Buma, M. Drabbels, IR spectroscopy of molecular ions by nonthermal ion ejection from helium nanodroplets. *J. Am. Chem. Soc.* **132**(40), 14086–14091 (2010). <https://doi.org/10.1021/ja1034655>
48. F. Bierau, P. Kupser, G. Meijer, G. von Helden, Catching proteins in liquid helium droplets. *Phys. Rev. Lett.* **105**(13):133402(2010) <https://doi.org/10.1103/PhysRevLett.105.133402>
49. M. Alghamdi, J. Zhang, A. Oswald, J.J. Porter, R.A. Mehl, W. Kong, Doping of green fluorescent protein into superfluid helium droplets: size and velocity of doped droplets. *J. Phys. Chem. A.* **121**(36), 6671–6678 (2017). <https://doi.org/10.1021/acs.jpca.7b05718>
50. L. Tiefenthaler, J. Ameixa, P. Martini, S. Albertini, L. Ballauf, M. Zankl, M. Goulart, F. Laimer, K. von Haefen, F. Zappa, P. Scheier, An intense source for cold cluster ions of a specific composition. *Rev. Sci. Instrum.* **91**(3) (2020) <https://doi.org/10.1063/1.5133112>
51. F. Filsinger, D.S. Ahn, G. Meijer, G. von Helden, Photoexcitation of mass/charge selected hemin<sup>+</sup>, caught in helium nanodroplets. *Phys. Chem. Chem. Phys.* **14**(38), 13370–13377 (2012). <https://doi.org/10.1039/c2cp42071f>
52. D.A. Thomas, M. Marianski, E. Mucha, G. Meijer, M.A. Johnson, G. von Helden, Ground-state structure of the proton-bound formate dimer by cold-ion infrared action spectroscopy. *Angew. Chem-Int. Edit.* **57**(33), 10615–10619 (2018). <https://doi.org/10.1002/anie.201805436>
53. D.A. Thomas, E. Mucha, S. Gewinner, W. Schollkopf, G. Meijer, G. von Helden, Vibrational spectroscopy of fluoroformate, FCO<sub>2</sub><sup>-</sup>, trapped in helium nanodroplets. *J. Phys. Chem. Lett.* **9**(9), 2305–2310 (2018). <https://doi.org/10.1021/acs.jpclett.8b00664>
54. D.A. Thomas, E. Mucha, M. Lettow, G. Meijer, M. Rossi, G. von Helden, Characterization of a trans-trans carbonic acid-fluoride complex by infrared action spectroscopy in helium nanodroplets. *J Am Chem Soc* **141**(14), 5815–5823 (2019). <https://doi.org/10.1021/jacs.8b13542>
55. V. Scutelnic, M.A.S. Perez, M. Marianski, S. Warnke, A. Gregor, U. Rothlisberger, M.T. Bowers, C. Baldauf, G. von Helden, T.R. Rizzo, J. Seo, The Structure of the protonated serine octamer. *J. Am. Chem. Soc.* **140**(24), 7554–7560 (2018). <https://doi.org/10.1021/jacs.8b02118>
56. M. Marianski, J. Seo, E. Mucha, D.A. Thomas, S. Jung, R. Schlogl, G. Meijer, A. Trunschke, G. von Helden, Structural characterization of molybdenum oxide nanoclusters using ion mobility spectrometry mass spectrometry and infrared action spectroscopy. *J. Phys. Chem. C* **123**(13), 7845–7853 (2019). <https://doi.org/10.1021/acs.jpcc.8b06985>
57. A.I. González Flórez, D.-S. Ahn, S. Gewinner, W. Schöllkopf, G. von Helden, IR spectroscopy of protonated leu-enkephalin and its 18-crown-6 complex embedded in helium droplets. *Phys. Chem. Chem. Phys.* **17**(34), 21902–21911 (2015). <https://doi.org/10.1039/C5CP02172C>
58. A.I. González Flórez, E. Mucha, D.-S. Ahn, S. Gewinner, W. Schöllkopf, K. Pagel, G. von Helden, Charge-induced unzipping of isolated proteins to a defined secondary structure. *Angew. Chem. Int. Ed.* **55**(10), 3295–3299 (2016). <https://doi.org/10.1002/ange.201510983>

59. D.A. Thomas, R. Chang, E. Mucha, M. Lettow, K. Greis, S. Gewinner, W. Schollkopf, G. Meijer, G. von Helden, Probing the conformational landscape and thermochemistry of DNA dinucleotide anions via helium nanodroplet infrared action spectroscopy. *Phys. Chem. Chem. Phys.* **22**(33), 18400–18413 (2020). <https://doi.org/10.1039/d0cp02482a>
60. E. Mucha, A.I. Gonzalez Florez, M. Marianski, D.A. Thomas, W. Hoffmann, W.B. Struwe, H.S. Hahm, S. Gewinner, W. Schollkopf, P.H. Seeberger, G. von Helden, K. Pagel, Glycan Fingerprinting via cold-ion infrared spectroscopy. *Angew. Chem.-Int. Edit.* **56**(37), 11248–11251 (2017). <https://doi.org/10.1002/anie.201702896>
61. E. Mucha, M. Lettow, M. Marianski, D.A. Thomas, W.B. Struwe, D.J. Harvey, G. Meijer, P.H. Seeberger, G. von Helden, K. Pagel, Fucose migration in intact protonated glycan ions: a universal phenomenon in mass spectrometry. *Angew. Chem-Int. Edit.* **57**(25), 7440–7443 (2018). <https://doi.org/10.1002/anie.201801418>
62. M. Lettow, E. Mucha, C. Manz, D.A. Thomas, M. Marianski, G. Meijer, G. von Helden, K. Pagel, The role of the mobile proton in fucose migration. *Anal. Bioanal. Chem.* **411**(19), 4637–4645 (2019). <https://doi.org/10.1007/s00216-019-01657-w>
63. M. Lettow, M. Grabarics, K. Greis, E. Mucha, D.A. Thomas, P. Chopra, G.J. Boons, R. Karlsson, J.E. Turnbull, G. Meijer, R.L. Miller, G. von Helden, K. Pagel, Cryogenic infrared spectroscopy reveals structural modularity in the vibrational fingerprints of heparan sulfate diastereomers. *Anal. Chem.* **92**(15), 10228–10232 (2020). <https://doi.org/10.1021/acs.analchem.0c02048>
64. M. Lettow, M. Grabarics, E. Mucha, D.A. Thomas, L. Polewski, J. Freyre, J. Rademann, G. Meijer, G. von Helden, K. Pagel, IR action spectroscopy of glycosaminoglycan oligosaccharides. *Anal. Bioanal. Chem.* **412**(3), 533–537 (2020). <https://doi.org/10.1007/s00216-019-02327-7>
65. E. Mucha, M. Marianski, F.F. Xu, D.A. Thomas, G. Meijer, G. von Helden, P.H. Seeberger, K. Pagel, Unravelling the structure of glycosyl cations via cold-ion infrared spectroscopy. *Nat. Commun.* **9**(1), 4174 (2018). <https://doi.org/10.1038/s41467-018-06764-3>
66. K. Greis, C. Kirschbaum, S. Lechnitz, S. Gewinner, W. Schollkopf, G. von Helden, G. Meijer, P.H. Seeberger, K. Pagel, Direct experimental characterization of the ferrier glycosyl cation in the gas phase. *Org. Lett.* **22**(22), 8916–8919 (2020). <https://doi.org/10.1021/acs.orglett.0c03301>
67. K. Greis, E. Mucha, M. Lettow, D.A. Thomas, C. Kirschbaum, S. Moon, A. Pardo-Vargas, G. von Helden, G. Meijer, K. Gilmore, P.H. Seeberger, K. Pagel, The impact of leaving group anomericity on the structure of glycosyl cations of protected galactosides. *ChemPhysChem.* **21**(17), 1905–1907 (2020). <https://doi.org/10.1002/cphc.202000473>
68. M. Marianski, E. Mucha, K. Greis, S. Moon, A. Pardo, C. Kirschbaum, D.A. Thomas, G. Meijer, G. von Helden, K. Gilmore, P.H. Seeberger, K. Pagel, remote participation during glycosylation reactions of galactose building blocks: direct evidence from cryogenic vibrational spectroscopy. *Angew. Chem.-Int. Ed.* **59**(15), 6166–6171 (2020). <https://doi.org/10.1002/anie.201916245>
69. C. Kirschbaum, E.M. Saied, K. Greis, E. Mucha, S. Gewinner, W. Schollkopf, G. Meijer, G. von Helden, B.L.J. Poad, S.J. Blanksby, C. Arenz, K. Pagel, Resolving sphingolipid isomers using cryogenic infrared spectroscopy. *Angew. Chem-Int. Edit.* **59**(32), 13638–13642 (2020). <https://doi.org/10.1002/anie.202002459>
70. C. Kirschbaum, K. Greis, E. Mucha, L. Kain, S.L. Deng, A. Zappe, S. Gewinner, W. Schöllkopf, G. von Helden, G. Meijer, P.B. Savage, M. Marianski, L. Teyton, K. Pagel, Unravelling the structural complexity of glycolipids with cryogenic infrared spectroscopy. *Nat. Comm.* **12**(1) (2021) <https://doi.org/10.1038/s41467-021-21480-1>
71. W. Schöllkopf, S. Gewinner, H. Junkes, A. Paarman, G. von Helden, H. Bluem, A.M.M. Todd, The new IR and THz FEL Facility at the Fritz Haber Institute in Berlin, in *Paper presented at the SPIE Optics + Optoelectronics* (2015)
72. J.M.J. Madey, Stimulated emission of bremsstrahlung in a periodic magnetic field. *J. Appl. Phys.* **42**(5), 1906 (1971). <https://doi.org/10.1063/1.1660466>

73. L.R. Elias, W.M. Fairbank, J.M.J. Madey, H.A. Schwettman, T.I. Smith, Observation of stimulated emission of radiation by relativistic electrons in a spatially periodic transverse magnetic-field. *Phys. Rev. Lett.* **36**(13), 717–720 (1976). <https://doi.org/10.1103/PhysRevLett.36.717>
74. K. Nauta, R. Miller, Metastable vibrationally excited HF ( $v=1$ ) in helium nanodroplets. *J. Chem. Phys.* **113**(21), 9466–9469 (2000)
75. A. Varki, R.D. Cummings, M. Aeby, N.H. Packer, P.H. Seeberger, J.D. Esko, P. Stanley, G. Hart, A. Darvill, T. Kinoshita, J.J. Prestegard, R.L. Schnaar, H.H. Freeze, J.D. Marth, C.R. Bertozzi, M.E. Etzler, M. Frank, J.F. Vliegthart, T. Lutteke, S. Perez, E. Bolton, P. Rudd, J. Paulson, M. Kanehisa, P. Toukach, K.F. Aoki-Kinoshita, A. Dell, H. Narimatsu, W. York, N. Taniguchi, S. Kornfeld, Symbol nomenclature for graphical representations of glycans. *Glycobiology* **25**(12), 1323–1324 (2015). <https://doi.org/10.1093/glycob/cwv091>
76. R.G. Cooks, D. Zhang, K.J. Koch, F.C. Gozzo, M.N. Eberlin, Chiroselective self-directed octamerization of serine: implications for homochirogenesis. *Anal. Chem.* **73**(15), 3646–3655 (2001). <https://doi.org/10.1021/ac010284i>
77. S.C. Naita, R.G. Cooks, Serine octamers: cluster formation, reactions, and implications for biomolecule homochirality. *Angew. Chem-Int. Edit.* **45**(4), 554–569 (2006). <https://doi.org/10.1002/anie.200501328>
78. T.B. McMahon, C.J. Northcott, The fluoroformate ion,  $\text{FCO}_2^-$ . An ion cyclotron resonance study of the gas phase lewis acidity of carbon dioxide and related isoelectronic species. *Can. J. Chem.* **56**(8), 1069–1074 (1978). <https://doi.org/10.1139/v78-181>
79. J.W. Larson, T.B. McMahon, Fluoride and chloride affinities of main group oxides, fluorides, oxofluorides, and alkyls. Quantitative scales of Lewis acidities from ion cyclotron resonance halide-exchange equilibria. *J. Am. Chem. Soc.* **107**(4), 766–773 (1985). <https://doi.org/10.1021/ja00290a005>
80. S.J. Blanksby, G.B. Ellison, Bond dissociation energies of organic molecules. *Acc. Chem. Res.* **36**(4), 255–263 (2003). <https://doi.org/10.1021/ar020230d>
81. B.S. Ault, Matrix isolation investigation of the fluoroformate anion. *Inorg. Chem.* **21**(2), 756–759 (1982). <https://doi.org/10.1021/ic00132a056>
82. X. Zhang, U. Gross, K. Seppelt, Fluorocarbonate,  $[\text{FCO}_2]^-$ : preparation and structure. *Angew. Chem. Int. Ed.* **34**(17), 1858–1860 (1995). <https://doi.org/10.1002/anie.199518581>
83. D.W. Arnold, S.E. Bradforth, E.H. Kim, D.M. Neumark, Study of halogen-carbon dioxide clusters and the fluoroformyl radical by photodetachment of  $\text{X}^-(\text{CO}_2)$  ( $\text{X}=\text{I}, \text{Cl}, \text{Br}$ ) and  $\text{F}_c\text{O}_2^-$ . *J. Chem. Phys.* **102**(9), 3493–3509 (1995). <https://doi.org/10.1063/1.468575>
84. L.J. Murphy, K.N. Robertson, S.G. Harroun, C.L. Brosseau, U. Werner-Zwanziger, J. Moilanen, H.M. Tuononen, J.A.C. Clyburne, A simple complex on the verge of breakdown: isolation of the elusive cyanofluoroformate ion. *Science* **344**(6179), 75–78 (2014). <https://doi.org/10.1126/science.1250808>
85. M. Torrent-Sucarrat, A.J.C. Varandas, Carbon dioxide capture and release by anions with solvent-dependent behaviour: a theoretical study. *Chem-Eur. J.* **22**(39), 14056–14063 (2016). <https://doi.org/10.1002/chem.201602538>
86. J.M. Weber, H. Schneider, Infrared spectra of  $\text{X}^-\cdot\text{CO}_2\cdot\text{Ar}$  cluster anions ( $\text{X}=\text{Cl}, \text{Br}, \text{I}$ ). *J. Chem. Phys.* **120**(21), 10056–10061 (2004). <https://doi.org/10.1063/1.1736633>
87. H.K. Gerardi, A.F. DeBlase, X. Su, K.D. Jordan, A.B. McCoy, M.A. Johnson, Unraveling the anomalous solvatochromic response of the formate ion vibrational spectrum: an infrared, Ar-tagging study of the  $\text{HCO}_2^-$ ,  $\text{DCO}_2^-$ , and  $\text{HCO}_2^-\cdot\text{H}_2\text{O}$  ions. *J. Phys. Chem. Lett.* **2**(19), 2437–2441 (2011). <https://doi.org/10.1021/jz200937v>
88. W. Schneider, W. Thiel, Anharmonic force fields from analytic second derivatives: method and application to methyl bromide. *Chem. Phys. Lett.* **157**(4), 367–373 (1989). [https://doi.org/10.1016/0009-2614\(89\)87263-X](https://doi.org/10.1016/0009-2614(89)87263-X)
89. J.F. Stanton, J. Gauss, Analytic second derivatives in high-order many-body perturbation and coupled-cluster theories: computational considerations and applications. *Int. Rev. Phys. Chem.* **19**(1), 61–95 (2000). <https://doi.org/10.1080/014423500229864>

90. J. Vázquez, J.F. Stanton, Simple(r) algebraic equation for transition moments of fundamental transitions in vibrational second-order perturbation theory. *Mol. Phys.* **104**(3), 377–388 (2006). <https://doi.org/10.1080/00268970500290367>
91. J.F. Stanton, J. Gauss, L. Cheng, M.E. Harding, D.A. Matthews, P.G. Szalay, PG CFOUR, coupled-cluster techniques for computational chemistry.
92. V. Barone, Anharmonic vibrational properties by a fully automated second-order perturbative approach. *J. Chem. Phys.* **122**(1):014108 (2005) <https://doi.org/10.1063/1.1824881>
93. V. Barone, J. Bloino, C.A. Guido, F. Lipparini, A fully automated implementation of VPT2 infrared intensities. *Chem. Phys. Lett.* **496**(1), 157–161 (2010). <https://doi.org/10.1016/j.cpl.2010.07.012>
94. M.J. Frisch, G.W. Trucks, H.B. Schlegel, G.E. Scuseria, M.A. Robb, J.R. Cheeseman, G. Scalmani, V. Barone, G.A. Petersson, H. Nakatsuji, X. Li, M. Caricato, A.V. Marenich, J. Bloino, B.G. Janesko, R. Gomperts, B. Mennucci, H.P. Hratchian, J.V. Ortiz, A.F. Izmaylov, J.L. Sonnenberg, Williams, F. Ding, F. Lipparini, F. Egidi, J. Goings, B. Peng, A. Petrone, T. Henderson, D. Ranasinghe, V.G. Zakrzewski, J. Gao, N. Rega, G. Zheng, W. Liang, M. Hada, M. Ehara, K. Toyota, R. Fukuda, J. Hasegawa, M. Ishida, T. Nakajima, Y. Honda, O. Kitao, H. Nakai, T. Vreven, K. Throssell, J.A. Montgomery Jr, J.E. Peralta, F. Ogliaro, M.J. Bearpark, J.J. Heyd, E.N. Brothers, K.N. Kudin, V.N. Staroverov, T.A. Keith, R. Kobayashi, J. Normand, K. Raghavachari, A.P. Rendell, J.C. Burant, S.S. Iyengar, J. Tomasi, M. Cossi, J.M. Millam, M. Klene, C. Adamo, R. Cammi, J.W. Ochterski, R.L. Martin, K. Morokuma, O. Farkas, J.B. Foresman, D.J. Fox, Gaussian 16 Rev. C.01. Wallingford, CT (2016)
95. A. Varki, Biological roles of oligosaccharides: all of the theories are correct. *Glycobiology* **3**(2), 97–130 (1993)
96. A. Varki, Biological roles of glycans. *Glycobiology* **27**(1), 3–49 (2016). <https://doi.org/10.1093/glycob/cww086>
97. R.A. Dwek, Glycobiology: toward understanding the function of sugars. *Chem. Rev.* **96**(2), 683–720 (1996). <https://doi.org/10.1021/cr940283b>
98. K.W. Moremen, M. Tiemeyer, A.V. Nairn, Vertebrate protein glycosylation: diversity, synthesis and function. *Nat. Rev. Mol. Cell Biol.* **13**(7), 448–462 (2012). <https://doi.org/10.1038/nrm3383>
99. M.M. Fuster, J.D. Esko, The sweet and sour of cancer: glycans as novel therapeutic targets. *Nat. Rev. Cancer* **5**(7), 526–542 (2005). <https://doi.org/10.1038/nrc1649>
100. O.C. Grant, D. Montgomery, K. Ito, R.J. Woods, Analysis of the SARS-CoV-2 spike protein glycan shield reveals implications for immune recognition. *Sci. Rep.* **10**(1), 14991 (2020). <https://doi.org/10.1038/s41598-020-71748-7>
101. L. Casalino, Z. Gaieb, J.A. Goldsmith, C.K. Hjorth, A.C. Dommer, A.M. Harbison, C.A. Fogarty, E.P. Barros, B.C. Taylor, J.S. McLellan, E. Fadda, R.E. Amaro, Beyond shielding: the roles of glycans in the SARS-CoV-2 spike protein. *ACS Cent. Sci.* **6**(10), 1722–1734 (2020). <https://doi.org/10.1021/acscentsci.0c01056>
102. Y. Watanabe, J.D. Allen, D. Wrapp, J.S. McLellan, M. Crispin, Site-specific glycan analysis of the SARS-CoV-2 spike. *Science* **369**(6501), 330–333 (2020). <https://doi.org/10.1126/science.abb9983>
103. A. Shajahan, N.T. Supekar, A.S. Gleinich, P. Azadi, Deducing the N- and O-glycosylation profile of the spike protein of novel coronavirus SARS-CoV-2. *Glycobiology* **30**(12), 981–988 (2020). <https://doi.org/10.1093/glycob/cwaa042>
104. D. Cremer, J.A. Pople, General definition of ring puckering coordinates. *J. Am. Chem. Soc.* **97**(6), 1354–1358 (1975). <https://doi.org/10.1021/ja00839a011>
105. Neelamegham S, Aoki-Kinoshita K, Bolton E, Frank M, Lisacek F, Lütke T, O’Boyle N, Packer NH, Stanley P, Toukach P, Varki A, Woods RJ, Updates to the symbol nomenclature for glycans guidelines. *Glycobiology* **29**(9), 620–624 (2019)<https://doi.org/10.1093/glycob/cwz045>
106. J. Hofmann, H.S. Hahm, P.H. Seeberger, K. Pagel, Identification of carbohydrate anomers using ion mobility-mass spectrometry. *Nature* **526**(7572), 241–244 (2015). <https://doi.org/10.1038/nature15388>

**Open Access** This chapter is licensed under the terms of the Creative Commons Attribution 4.0 International License (<http://creativecommons.org/licenses/by/4.0/>), which permits use, sharing, adaptation, distribution and reproduction in any medium or format, as long as you give appropriate credit to the original author(s) and the source, provide a link to the Creative Commons license and indicate if changes were made.

The images or other third party material in this chapter are included in the chapter's Creative Commons license, unless indicated otherwise in a credit line to the material. If material is not included in the chapter's Creative Commons license and your intended use is not permitted by statutory regulation or exceeds the permitted use, you will need to obtain permission directly from the copyright holder.

